Enhanced Intersystem Crossing via a High Energy Charge Transfer State in a Perylenediimide−Perylenemonoimide Dyad

Dirk Veldman, Stéphanie M. A. Chopin, Stefan C. J. Meskers, and René A. J. Janssen*

Molecular Materials and Nanosystems, Eindhoven University of Technology, P.O. Box 513, Eindhoven, NL-5600 MB, The Netherlands

Received: July 6, 2008

The electronic relaxation processes of a photoexcited linear perylenediimide−perylenemonoimide (PDI-PMI) acceptor−donor dyad were studied. PDI-PMI serves as a model compound for donor−acceptor systems in photovoltaic devices and has been designed to have a high-energy $PDI^{-\bullet}$-$PMI^{+\bullet}$ charge transfer (CT) state. Our study focuses on the minimal Gibbs free energy (ΔG_{ET}) required to achieve quantitative CT and on establishing the role of charge recombination to a triplet state. We used time-resolved photoluminescence and picosecond photoinduced absorption (PIA) to investigate excited singlet (S_1) and CT states and complemented these experiments with singlet oxygen ($^1\Delta_g$) luminescence and PIA measurements on longer timescales to study the population of triplet excited states (T_1). In an apolar solvent like cyclohexene (CHX), photoinduced electron transfer does not occur, but in more polar solvents such as toluene (TOL) and chlorobenzene (CB), photoexcitation is followed by a fast electron transfer, populating the $PDI^{-\bullet}$-$PMI^{+\bullet}$ CT state. We extract rate constants for electron transfer (ET; $S_1 \rightarrow CT$), back electron transfer (BET; $S_1 \leftarrow CT$), and charge recombination (CR) to lower-energy states ($CT \rightarrow S_0$ and $CT \rightarrow T_1$). Temperature-dependent measurements yield the barriers for the transfer reactions. For ET and BET, these correspond to predictions from Marcus−Jortner theory and show that efficient, near quantitative electron transfer ($k_{ET}/k_{BET} \geq 100$) can be obtained when $\Delta G_{ET} \approx -120$ meV. With respect to triplet state formation, we find a relatively low triplet quantum yield ($\Phi_T < 25\%$) in CHX but much higher values ($\Phi_T = 30-98\%$) in TOL and CB. We identify the $PDI^{-\bullet}$-$PMI^{+\bullet}$ state as a precursor to the T_1 state. Recombination to T_1, rather than to the ground-state S_0, is required to rationalize the experimental barrier for CR. Finally, we discuss the relevance of these results for electron donor−acceptor films in photovoltaic devices.

Introduction

The active layer of the most efficient polymer solar cells to date consists of a partially phase-separated blend of a p-type (electron donating, D) conjugated semiconducting polymer and an n-type (electron accepting, A) material, which can be a small molecule, a second conjugated polymer, or an inorganic nanocrystalline semiconductor.[1] Light absorption results in a bound electron−hole pair (exciton) in either of the two materials. After diffusion of the exciton to the D−A interface, the first step in the charge separation process is an electron transfer step between D and A, creating a charge transfer (CT) state in which D and A are positively and negatively charged, respectively. The CT state, which can be described as a weakly bound electron−hole pair at the D−A interface, must be further dissociated to allow efficient collection of electrons and holes at the opposite electrodes.

For efficient conversion of sunlight into electrical power, the photoinduced CT reaction should be both quantum *and* energy efficient, that is, the process $S_1 \rightarrow CT$ should occur with unit quantum yield and minimal energy loss [$E(S_1) \approx E_{CT}$]. The first condition enables a high photocurrent, and the second condition enables a high photovoltage because E_{CT} determines the maximum attainable open-circuit voltage (V_{OC}). A third requirement for efficient power conversion is that the lifetime of the CT state is long enough to allow efficient spatial separation and eventually the collection of the electrons and holes. Because the driving force for electron transfer reactions $\Delta G_{ET} = E_{CT} - E(S_1)$ is one of the parameters that determines the forward rate and efficiency of electron transfer, the question arises whether the desired combination of high quantum *and* high energy efficiency exists in photoinduced electron transfer. This is one of the questions that we address here.

For photovoltaic blends, it has been suggested that a driving force of $\Delta G_{ET} \approx -0.35$ eV from the lowest singlet excited state is required for full electron transfer from D to A.[2,3] However, these estimates are based on approximations of E_{CT}—for example, obtained from the oxidation potentials and the optical band gaps of the materials—because a more direct measure of E_{CT} can often not be obtained.[3]

Covalently linked molecular D−A dyads can be seen as model compounds for D−A blends used in solar cells. In such a D−A dyad, photoexcitation of D or A is followed by electron transfer, populating a CT state, which can be described in the first approximation as a radical ion pair with the radical cation ($D^{\bullet+}$) and the radical anion ($A^{\bullet-}$) interacting to a degree determined by their electronic coupling. Sometimes, the energy of this state, E_{CT}, can be determined from CT emission. Alternatively, E_{CT} can be predicted by point-dipole estimations.[4]

Information about the third requirement of a CT state in a D−A blend used for photovoltaics, that is, the long lifetime, can be inferred from transient absorption[5,6] or CT (or exciplex) emission studies.[7−12] Both reveal that charge recombination, either geminate or nongeminate, often occurs in the nanosecond

* To whom correspondence should be addressed. E-mail: r.a.j.janssen@tue.nl.

10.1021/jp805949r CCC: $40.75
Published on Web 08/27/2008

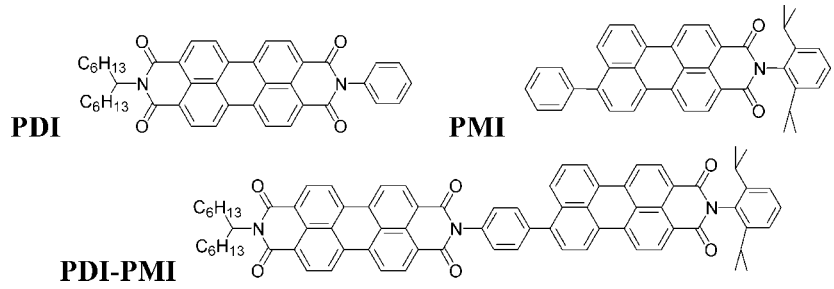

Figure 1. Structures of PDI-PMI and the reference compounds PDI and PMI.

time domain. Recently, enhanced triplet formation via a CT state has been reported in some D−A blends used for organic photovoltaics,[12−14] a process that is recognized as a loss mechanism because it involves the recombination of photoexcited charge carriers and, hence, a reduced photocurrent. It is obvious that such charge recombination can only occur if E_{CT} is similar to—or higher than—$E(T_1)$, the energy of the lowest charge neutral triplet excited state (T_1) of D or A. Especially, in designing conjugated D−A molecules or materials where E_{CT} is close to $E(S_1)$,[15] the condition that $E_{CT} > E(T_1)$ will likely occur because the exchange energy $E(S_1) - E(T_1)$ of conjugated molecules can be up to 1 eV. Very recently, quantum chemical calculations have shown that the electronic coupling between CT and intramolecular triplet states in D−A pairs can be similar to those arising from associated intramolecular singlet states.[16] However, detailed experimental information on the triplet formation process—such as rates, yields, transfer barriers, and the mechanism of formation—in D−A blends is lacking. Again, the properties of this triplet state formation are difficult to study in such blend films due to, for example, structural disorder inside these blends. Crucial insights, however, can be obtained from D−A dyads.

The process of populating T_1 from a CT state and vice versa has been extensively studied for such D−A model compounds. It is now well-established that one of the prerequisites to realize CT states with long (i.e., in the microsecond range) lifetimes in artificial systems mimicking the (bacterial) photosynthetic unit is that charge recombination to a locally excited triplet state should be prevented, as pointed out in a recent review by Verhoeven.[17] The electronic coupling between D and A is reduced exponentially with ion separation distance. At long D−A pair separation ($R_{CC} > 15$ Å),[18] and hence very weak electronic coupling, radical pair intersystem crossing (RP-ISC) is the commonly observed mechanism of triplet formation from CT states.[19−22] Here, ISC occurs from the initially singlet excited CT state to—due to the weak coupling between the CT states—the nearly degenerate triplet CT state ($^1CT \rightarrow {}^3CT$), mainly via hyperfine interaction (HFI)-driven spin dephasing. For weakly coupled states at ambient temperature, that process occurs typically on the order of 10 ns. The slow ISC is followed by a fast charge recombination populating the locally excited triplet state ($^3CT \rightarrow T_1$). RP-ISC is the main process in the photosynthetic reaction center[21] and is commonly observed for D−A−A triads.[22] For D−A pairs at a much shorter separation distance, ISC via HFI, thus via RP-ISC, is less obvious, because the much stronger electronic coupling between D and A causes the energy splitting between ^1CT and ^3CT to become larger than the HFI energy. Still, also for much shorter molecular D−A dyads, rapid ISC via the CT state was observed upon photoexcitation. Such dyads include pyrene−amine,[23] porphyrine−quinone,[19] methylacridinium ions,[24,25] bodipy-*N*-methylpyridinium,[26] small monoimide−diimide dyads,[20] perylenemonoimide (PMI)−triphenylamine,[27,28] and a porphyrin−C_{60} dyad.[29] The ISC rates ($CT \rightarrow T_1$) for these dyads are generally in the range of 0.01−1 ns^{-1},[23,25,26,29,30] while for pyrene−amine in hexane an even faster rate (>20 ns^{-1}) is reported.[23] An alternative decay pathway for photoinduced CT states of dyads with strong electronic coupling between the anion and the cation is a direct conversion ($^1CT \rightarrow T_1$) via spin−orbit coupling (SO-ISC), involving a coupled electron transfer and spin inversion.[23,24] Such a process is enhanced by a nearly perpendicular orientation of the donor and acceptor units.[31] Recently, Dance et al. reported on ISC at low temperature in donor−bridge−acceptor (D−B−A) systems comprised of a phenothiazine (D) and a perylenediimide (PDI) (A) and found that for short bridge (B) length—one phenyl ring—SO-ISC mainly occurs, while for longer bridge lengths (2−5 phenyl groups), RP-ISC is the main contributor of the ISC process.[18] In addition to CT states as precursors for T_1, also higher lying excited states have been shown to play a role in PMI derivatives.[32,33]

In this study, we focus on a new electron D−A system, PDI-PMI (Figure 1), that serves as a model for a system with a low ΔG_{ET} [and hence $E_{CT} \approx E(S_1)$] in an environment [e.g., toluene (TOL)] of low relative permittivity (ε_r). PDI-PMI is a rigid linear dyad of PDI and PMI coupled with one phenyl ring, and its photophysical properties are compared to PDI and PMI that are structurally similar but carry only one of the two chromophores. According to density functional theory (DFT) calculations, the dihedral angles of the bridging phenyl with the PDI and PMI chromophores in PDI-PMI are about 70°[34] and 60°,[35] respectively. Together with the node in the frontier orbitals on the imide nitrogen in PDI, this causes delocalization of π-electrons through the bridge to be minimal. Reasons to choose perylenemides as model compounds are their high fluorescence quantum yields, chemical inertness, and photochemical stability. They are well-soluble if so-called swallow tails or substituted phenyl moieties are introduced.[36] Other examples of linear dyads containing PDI and PMI molecules are PDI-PDI,[37−40] PMI-PMI,[41] and another PDI-PMI.[42]

The photoinduced electron transfer processes, populating intramolecular CT states, have been thoroughly investigated for a number of these dyads and show interesting features. For example, a strong distance and solvent dependence is observed for the equilibrium between a fluorescent and a CT state for the PDI-PDI dyads[38,40] and also for PMI-triphenylamine dyads.[27,43] Studies on the electron transfer barriers, however, and on the triplet excited-state population have not been reported. After photoexcitation of PDI-PMI and relaxation of the molecule to the lowest fluorescent singlet excited state (S_1), the electronic processes can be described by fluorescence (k_F), nonradiative decay (k_{NR}), electron transfer (k_{ET}), back electron transfer (k_{BET}), and charge recombination (k_{CR}), as schematically shown in Figure 2a.

The PDI-PMI dyad is interesting as a model for blends of conjugated materials used as the photoactive layer in organic photovoltaic devices, because it has the following properties:

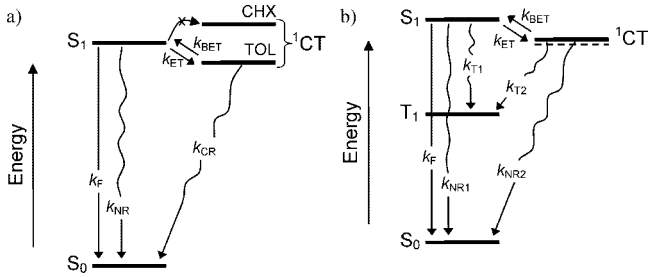

Figure 2. (a) Schematic drawing with the relative energies of the lowest fluorescent singlet excited (S_1, ^{1}PDI*-PMI or PDI-^{1}PMI*), the CT state (^{1}CT, PDI$^{-\bullet}$-PMI$^{+\bullet}$) in cyclohexene (CHX) and TOL, and the singlet ground state (S_0), and the transfer rates between these states: fluorescence (k_F), nonradiative decay (k_{NR}), electron transfer (k_{ET}), back electron transfer (k_{BET}), and charge recombination (k_{CR}). (b) In addition to panel a, the lowest locally excited triplet excited (T_1) and CT (^{3}CT) states and the nonradiative decay rates to S_0 (k_{NR1} and k_{NR2}) or T_1 (k_{T1} and k_{T2}) are included.

(i) It consists of two conjugated systems, both of which are absorbing visible light; (ii) photoexcitation of either of the two chromophores populates a singlet excited state with an intrinsic decay time of a few nanoseconds; (iii) the chromophores are positioned at relatively short electron−hole separation distance; (iv) in a relatively apolar medium and at room temperature, the CT state is located just below S_1; and (v) the PDI unit possesses a low-energy triplet excited state [$E(T_1) = 1.2$ eV].[44] With all of these properties, it mimics those of organic donor−acceptor blends. Furthermore, the fact that the triplet excited state of monomeric PDI is only marginally populated (<0.5%) by direct photoexcitation is convenient, because it simplifies studying effects on the ISC rate.[45] Therefore, this dyad can give us a more profound insight in the charge separation and recombination processes occurring in photovoltaic devices.

In this paper, we describe the photophysical processes that occur following photoexcitation of PDI-PMI in a number of solvents and as a function of temperature, and we discuss the results focusing on two aspects: (i) the minimal driving force for electron transfer (ΔG_{ET}) that still allows quantitative CT, while achieving a maximum energy of the CT state, and (ii) the rate of ISC from the singlet CT state. We use Marcus−Jortner theory in combination with a continuum model for describing the energetics and to quantify the forward and backward electron transfer between the S_1 and the CT states and the recombination of CT to T_1 and S_0. Finally, the relevance of these results is discussed for D−A blend films for photovoltaic devices.

Experimental Section

General. All reagents and solvents were used as received or purified using standard procedures. Compounds PDI,[46] **1**,[47] and **3**[48] were synthesized following previously reported synthetic procedures. Column chromatography was performed using Merck silica gel 60 (230−240 mesh). ^{1}H NMR and ^{13}C NMR spectra were recorded at room temperature on a Varian Mercury (400 and 100 MHz, respectively). Proton chemical shifts are reported in ppm relative to tetramethylsilane (TMS). Infrared (FT-IR) spectra were recorded on a Perkin-Elmer Spectrum One UATR FT-IR spectrophotometer. Matrix-assisted laser desorption/ionization time-of-flight (MALDI-TOF) MS spectra were recorded on a Perspective DE Voyager spectrometer using α-cyano-4-hydroxycinnamic acid or 2-[(2*E*)-3-(4-*tert*-butylphenyl)-2-methylprop-2-enylidene]malononitrile (DCTB) as a matrix. Elemental analyses were carried out using a PerkinElmer 2400.

PMI. A mixture of *N*-(2,6-diisopropylphenyl)-9-bromoperylene-3,4-dicarboximide (**1**) (100 mg, 0.18 mmol), phenylboronic acid pinacol ester (28 mg, 0.23 mmol), and $Pd(PPh_3)_4$ (18.5 mg, 0.016 mmol, 9 mol%) was dissolved in 10 mL of TOL and 2 mL of 2 N K_2CO_3. The reaction mixture was stirred at 115 °C for 24 h. The solution was then poured into diluted HCl (200 mL) and extracted with CH_2Cl_2. The organic layer was dried over $MgSO_4$, followed by evaporation of the solvent. The crude product was carefully purified by silica gel column chromatography (CH_2Cl_2) to give PMI as a red solid (10 mg, 10%). IR: ν (cm^{-1}) 1698, 1660 ($\nu_{C=O}$ imide). ^{1}H NMR ($CDCl_3$, 400 MHz): δ 8.69−8.67 (2d, $J = 8$ Hz, 2H), 8.56−8.49 (m, 4H), 8.20 (d, $J = 8$ Hz, 1H), 7.63−7.46 (m, 8H), 7.36−7.34 (m, 2H), 2.78 (hept, $J = 6.8$ Hz, 2H), 1.19 (d, $J = 6.8$ Hz, 12H). ^{13}C NMR ($CDCl_3$, 100 MHz): δ 164.0, 145.7, 143.4, 137.8, 137.6, 132.7, 132.1, 132.0, 130.0, 129.5, 129.4, 128.6, 128.5, 128.3, 128.0, 127.0, 126.9, 124.0, 123.9, 123.6, 121.0, 120.9, 120.3, 120.1, 29.1, 24.0.; MALDI-TOF MS (*m*/*z*) calcd for $C_{40}H_{31}NO_2$, 557.24; found, $[M^\bullet]^+ = 557.1$.

N-(2,6-Diisopropylphenyl)-9-bromoperylene-3,4-dicarboximide (**1**) (100 mg, 0.18 mmol), 4-aminophenylboronic acid pinacol ester (50 mg, 0.23 mmol), and $Pd(PPh_3)_4$ (18 mg, 0.016 mmol, 9 mol%) were dissolved in 10 mL of TOL and 2 mL of 2 N K_2CO_3. The reaction mixture was stirred at 115 °C for 15 h. The solution was then poured into diluted HCl (200 mL) and extracted with CH_2Cl_2. The organic layer was dried over $MgSO_4$, followed by evaporation of the solvent. The crude product was carefully purified 2× by silica gel column chromatography (CH_2Cl_2) to give **2** as a dark purple solid (79 mg, 78%). IR: ν (cm^{-1}) 3372 (NH_2), 1695, 1657 ($\nu_{C=O}$ imide). ^{1}H NMR ($CDCl_3$, 400 MHz): δ 8.65−8.63 (2d, $J = 8$ Hz, 2H), 8.48−8.41 (m, 4H), 8.10 (d, $J = 7.6$ Hz, 1H), 7.61−7.57 (m, 2H), 7.48 (t, $J = 7.8$ Hz, 1H), 7.39−7.34 (m, 4H), 6.90 (d, $J = 8$ Hz, 2H), 2.78 (hept, $J = 6.8$ Hz, 2H), 1.19 (d, $J = 7.6$ Hz, 12H). ^{13}C NMR ($CDCl_3$, 100 MHz): δ 164.0, 146.4, 145.7, 143.8, 137.9, 137.8, 132.8, 132.1, 132.0, 131.1, 130.6, 129.8, 129.4, 129.3, 128.4, 128.1, 127.8, 126.9, 126.8, 124.0, 123.9, 123.8, 120.9, 120.5, 120.1, 119.8, 115.0, 29.7, 29.1, 24.0. MALDI-TOF MS (*m*/*z*) calcd for $C_{40}H_{32}N_2O_2$, 572.25; found, $[M + H]^+ = 573.2$.

PDI-PMI. A mixture of **2** (30 mg, 52.38 μmol), **3** (30.05 mg, 53.16 μmol), and imidazole (596 mg) was heated at 160 °C for 2 h. The crude product was purified by silica gel column chromatography (CH_2Cl_2) to give PDI-PMI as a dark red solid (33 mg, 56%). IR: ν (cm^{-1}) 1703, 1661 ($\nu_{C=O}$ imide). ^{1}H NMR ($CDCl_3$, 400 MHz): δ 8.77 (2d, $J = 8.4$ Hz, 2H), 8.69−8.62 (m, 8H), 8.56−8.46 (m, 4H), 8.17 (d, $J = 8$ Hz, 1H), 7.78 (d, $J = 8$ Hz, 2H), 7.72 (d, $J = 8$ Hz, 1H), 7.65 (t, $J = 8$ Hz, 1H), 7.59 (d, $J = 8$ Hz, 2H), 7.49 (t, $J = 7.8$ Hz, 1H), 7.36 (d, $J = 8$ Hz, 2H), 5.26−5.17 (m, 1H), 2.78 (hept, $J = 6.8$ Hz, 2H), 2.31−2.25 (m, 2H), 1.92−1.85 (m, 2H), 1.34−1.20 (m, 28H), 0.84 (t, $J = 7.0$ Hz, 6H). ^{13}C NMR ($CDCl_3$, 100 MHz): δ 163.9 (C═O), 163.6 (C═O), 145.7, 142.4, 140.3, 137.6, 137.4, 135.3, 134.9, 134.2, 132.5, 132.04, 132.04, 131.9, 131.0, 130.5, 129.8, 129.5, 129.4, 129.3, 128.9, 128.8, 128.4, 128.3, 127.2, 126.9, 126.7, 126.4, 124.0, 123.5, 123.4, 123.1, 123.0, 121.0, 120.9, 120.3, 120.2, 54.8, 32.4, 31.7, 29.7, 29.6, 29.2, 29.1, 26.9, 24.0, 22.6, 14.0. MALDI-TOF MS (*m*/*z*) calcd for $C_{77}H_{65}N_3O_6$, 1127.49; found, $[M^\bullet]^- = 1127.6$. Anal. calcd: C, 81.96; H, 5.81; N, 3.72; O, 8.51. Found: C, 80.36; H, 6.33; N, 3.43.

Electrochemistry. Cyclic voltammograms were recorded in an inert atmosphere with 0.1 M tetrabutylammonium hexafluorophosphate ($TBAPF_6$) in dichloromethane (DCM) as a supporting electrolyte. The working electrode was a platinum disk

(0.2 cm^2), and the counter electrode was a platinum electrode. The scan was performed using a Ag/AgCl reference electrode with a ferrocene−ferrocenium couple (Fc/Fc^+) as an internal standard (+0.35 V vsAg/AgCl in DCM) using a μAutolab II with a PGSTAT30 potentiostat and a scan speed of 100 mV/s.

Absorbance and Fluorescence. The solvents for spectroscopic studies were spectroscopic grade and used as received unless stated otherwise. UV/vis absorption spectra were recorded using a PerkinElmer Lambda 900 spectrophotometer, and steady state fluorescence spectra were recorded on an Edinburgh Instruments FS920 double-monochromator spectrophotometer with a Peltier-cooled red-sensitive photomultiplier. The emission spectra were corrected for the wavelength dependence of the sensitivity of the detection system. Time-correlated single photon counting fluorescence studies were performed on an Edinburgh Instruments LifeSpec-PS spectrometer by photoexcitation with a 400 nm picosecond laser (PicoQuant PDL 800B) operated at 2.5 MHz and detection with a Peltier-cooled Hamamatsu microchannel plate photomultiplier (R3809U-50). The data were deconvoluted with the instrument response function of the instrument, recorded using dispersed light, and fitted to a multiexponential function using the Fluofit package (PicoQuant, Berlin). Low-temperature (<300 K) fluorescence spectra were recorded using an Oxford Instruments nitrogen flow (CF) cryostat connected to an Oxford ITC601 temperature controller. A Lauda RC 20 CS refrigerated bath circulator was used to measure at temperatures above 300 K. The long component in the time traces of PDI-PMI in chlorobenzene—and the residual fluorescence in the steady state measurement—may be partly due to a fluorescent impurity, which causes a higher uncertainty in the values of k_{CR} and k_{BET} determined at this temperature.[49]

Subpicosecond Pump−Probe Photoinduced Absorption (ps-PIA). The femtosecond laser system consisted of an amplified Ti/sapphire laser (Spectra Physics Hurricane), providing 150 fs pulses at 800 nm with an energy of 750 μJ and a repetition rate of 1 kHz. The pump pulses at 490 nm were created via optical parametric amplification (OPA) of the 800 nm and frequency doubling. The probe beams at 540 and 955 nm were generated in a separate OPA. The pump beam was linearly polarized at the magic angle (54.7°) with respect to the probe beam, to cancel out orientation effects in the measured dynamics. The temporal evolution of the differential transmission was recorded using a Si detector by a standard lock-in technique at 500 Hz. For the ps-PIA as well as the ns-PIA (below), the solutions were placed in an airtight screw-cap quartz cuvette (Spectrocell) with 1 mm optical path length.

Nanosecond Pump−Probe PIA (ns-PIA). The spectra were recorded by exciting the sample with pulses at 488 nm (pulse width, 4 ns; repetition rate, 10 Hz) obtained from an optical parametric oscillator (OPO), pumped by the third harmonic of a Nd:YAG laser. An intensified charge-coupled device (CCD) camera was used to record the transmission of a tungsten−halogen probe light through the sample after dispersion by a spectrograph. The signal acquisition by the CCD camera was electronically gated at different time delays after the excitation pulse, with a gate width of 60 ns. To obtain differential transmission spectra, the reference transmission was recorded at a 20 ms delay. For the ns-PIA experiments, oxygen-free saturated solutions were prepared in a glovebox ($[O_2]$ < 10 ppm) unless stated otherwise and kept in a screw-capped quartz cell (Spectrocell) with an optical path length of 1 mm.

Oxygen Phosphorescence. For the singlet ($^1\Delta_g$) oxygen phosphorescence measurements, the spectra were recorded by exciting the sample with the second harmonic of a Nd:YAG laser (5 ns, 532 nm, 10 Hz repetition rate). The incoming beam was filtered with a 532 nm laser line filter (Lot Oriel), and the luminescence was collected at a straight angle to the excitation beam with a liquid N_2-cooled ultrasensitive germanium detector (Edinburgh Instruments EI-P) with an RG1000 (Schott) glass filter and a 1292 nm NIR band (T = 60% at 1270 nm, fwhm = 80 nm) pass filter (Lot Oriel). The diode signals were transferred to a PC and averaged 96 times. The samples were air-saturated solutions with absorbances amounting to 0.35 ± 0.01 at 532 nm, in a quartz cell with an optical path length of 10 mm.

Singlet oxygen ($^1\Delta_g$) quantum yields (Φ_Δ) were determined by probing the oxygen ($^1\Delta_g$) phosphorescence decay with time (see the Supporting Information, Figure S1) using[50,51]

$$\Phi_\Delta = \frac{n^2 I_P^0 k_P(\mathrm{ST})}{n^2(\mathrm{ST}) I_P^0(\mathrm{ST}) k_P} \Phi_\Delta(\mathrm{ST}) \quad (1)$$

with n the refractive index of the solvent, I_P^0 the extrapolated phosphorescence intensity at $t = 0$, and k_P the rate of radiative decay from the singlet oxygen ($^1\Delta_g$) state, taken from Scurlock et al.,[51] who reported k_P relative to that in benzene ($k_P' = k_P/k_P^{benzene}$). For CHX, k_P' is determined from the relation with the polarizability of the solvent ($k_P' = 0.68$).[51] ST denotes "standard": Here, C_{60} in benzene with $\Phi_\Delta = 0.95 \pm 0.05$.[52,53] The optical density was 0.35 ± 0.01 at 532 nm for each measurement.

We checked the experimental procedure using TPP (*meso*-tetraphenylporphyrin) as a reference compound. For TPP, the measured yields ($\Phi_\Delta = 0.70$ in benzene, and $\Phi_\Delta = 0.57$ in CB) show good correspondence to those determined previously in benzene ($\Phi_\Delta = 0.62$ and 0.78)[50,54] and in CB ($\Phi_\Delta = 0.61$).[50] The laser fluence dependence was carefully checked in each experiment (see the Supporting Information, Figure S1 and Table S1), and we found that only at laser fluences above 6 J m^{-2} the intensity of the signal starts to deviate from linearity.[55] At low fluences and after ~15 μs delay, the signal intensity has a decay rate that is equal for each compound in the same solvent (Figure S1 of the Supporting Information for TOL). From this decay, Φ_Δ was determined. At early times (<15 μs), the TPP and notably the PDI-PMI decay traces reveal additional short components that are absent in the C_{60} trace for which only a rise of the oxygen ($^1\Delta_g$) luminescence is observed. These short components are probably caused by saturation of the detector by residual photoluminescence, extending into the near-infrared.[56,57]

Results and Discussion

Synthesis of PDI-PMI. The bromo-substituted PMI **1**[47] was converted into the amine **2** via a Suzuki reaction by applying the commercially available 4-aminophenylboronic acid pinacol ester (Scheme 1).[58] Thereafter, **2** was reacted with **3**,[48] leading to PDI-PMI. Reference compound PMI was obtained from **1** by a Suzuki reaction with phenylboronic acid pinacol ester (Scheme 1). The low isolated yield in this step is due to the tedious separation from *N*-(2,6-diisopropylphenyl)perylene-3,4-dicarboximide, which also formed during the reaction. As a result of their solubilizing groups, PDI-PMI, PDI, and PMI are well-soluble in organic solvents such as DCM, TOL, chloroform, and tetrahydrofuran, allowing detailed characterization and analysis of their photophysical properties.

Electrochemistry. In Figure 3, the cyclic voltammogram of PDI-PMI in DCM is shown together with those of the reference compounds PDI and PMI. Comparison with the reference compounds reveals that the four reversible reduction waves of PDI-PMI correspond to two reversible reductions of the PDI

SCHEME 1: Synthesis of PDI-PMI and PMI[a]

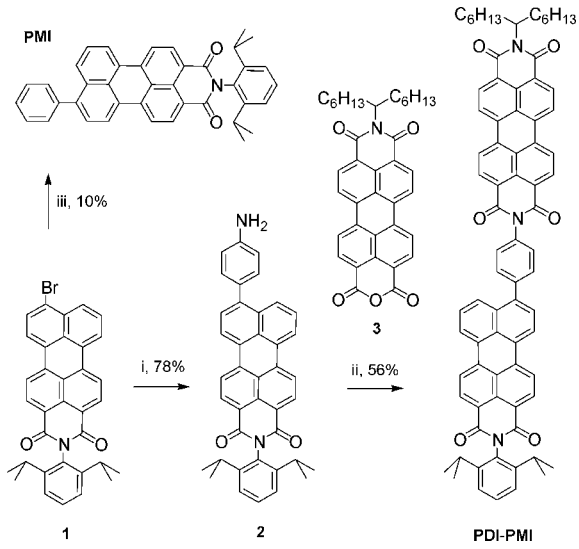

[a] Conditions: (i) A 1.3 equiv amount of 4-aminophenylboronic acid pinacol ester, 9% $Pd(PPh_3)_4$, TOL, 2 N potassium carbonate, 15 h, 115 °C. (ii) A 1.0 equiv amount of **3**, imidazole, 160 °C, 2 h. (iii) A 1.3 equiv amount of phenylboronic acid pinacol ester, 9% $Pd(PPh_3)_4$, TOL, 2 N potassium carbonate, 24 h, 115 °C.

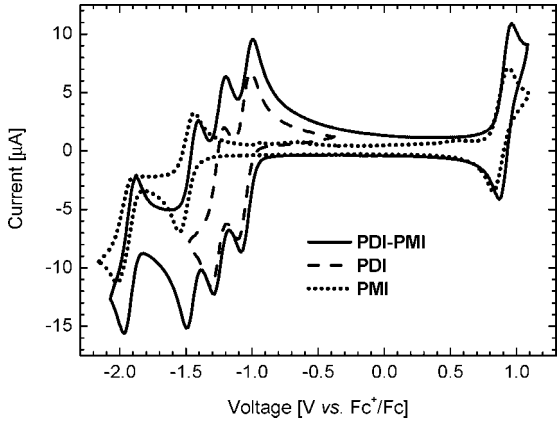

Figure 3. Cyclic voltammograms of PDI-PMI and the reference compounds PDI and PMI in DCM.

TABLE 1: Oxidation and Reduction Potentials in *V* vs Fc/Fc^+ Measured with a Scan Rate of 100 mV/s in DCM with 0.1 M $TBAPF_6$ as a Supporting Electrolyte

	E_{red}^4	E_{red}^3	E_{red}^2	E_{red}^1	E_{ox}^1
PDI			−1.260	−1.060	+1.25[a]
PMI			−1.950	−1.495	+0.885
PDI-PMI	−1.925	−1.450	−1.240	−1.040	+0.915

[a] Onset of oxidation.

moiety followed by two reductions of the PMI moiety (Table 1). The oxidation of PDI-PMI reveals one reversible peak, which results from the oxidation of the PMI part of the molecule. PDI is not oxidized up to +1.25 V vs Fc/Fc^+.[40] From these measurements, it is evident that for PDI-PMI the first reduction peak involves the formation of the PDI anion [E^o(PDI-PMI/PDI^--PMI) = −1.040 V vs Fc/Fc^+], while the first oxidation involves the PMI moiety [E^o(PDI-PMI/PDI-PMI^+) = +0.915 V vs Fc/Fc^+]. The energy difference between oxidation and reduction of PDI-PMI hence amounts to 1.95 eV in DCM.

Absorbance and Steady State Fluorescence at $T = 300$ K. The absorbance and fluorescence spectra and fluorescence quantum yields of PDI-PMI and the reference compounds PDI and PMI were determined in solvents of increasing polarity: CHX, TOL, and CB. PDI and PMI show very similar absorption and emission spectra with a vibronic progression and high fluorescence quantum yields (Φ_F, Table 2 and Figure 4). There are, however, some differences: (i) The vibronic peaks in the absorbance and emission spectra of PMI are broader than those of PDI and hence less resolved, (ii) the 0−0 vibronic absorption peak of PMI is 15 nm blue-shifted as compared to PDI, (iii) the emission spectra of PMI are 9−26 nm red-shifted from the spectra of PDI, and (iv) in the same solvent Φ_F is about 15% lower for PMI than for PDI for which $\Phi_F \sim 1$. We note that for a dendrimer-substituted PMI derivative, $\Phi_F = 0.95 \pm 0.05$ has been reported.[59] The difference is consistent with the excited state lifetime of 3.85 (PMI in TOL, Table 2) vs 4.25 ns (ref 59) and suggests that some weak nonradiative decay mechanism is active in PMI. Its origin is not clear but might involve intramolecular motion of the phenyl ring, which is easier in PMI than in the dendrimer-substituted PMI.

PDI-PMI shows an absorption that is similar to the sum of the PDI and PMI reference compounds (dashed line in Figure 4). Only the spectrum of the dyad is slightly red-shifted with respect to both PDI and PMI. The extinction coefficient at the maximum absorption is $\varepsilon = 98000$ L mol^{-1} cm^{-1} (PDI, 529 nm), $\varepsilon = 28000$ L mol^{-1} cm^{-1} (PMI, 520 nm), and $\varepsilon = 136000$ L mol^{-1} cm^{-1} (PDI-PMI, 533 nm) in DCM, respectively. Hence, the extinction coefficient of PDI-PMI is 8% higher than the sum of the two separate moieties. Both the red shift and the increased intensity of the 0−0 peak can be explained in terms of a weak excitonic coupling between the two chromophores.[37,60] This agrees with a marginally faster radiative decay rate (k_{rad}) for PDI-PMI than for the individual chromophores (Table 2). Additionally, the fact that the absorption spectrum of PDI-PMI largely resembles the sum of the two individual chromophores indicates that delocalization of π-electrons through the phenyl bridge is small.

The maximum of the fluorescence emission of PDI-PMI is at a wavelength intermediate to those of PDI and PMI (Table 2), and the spectral shape, although slightly broader than that of PDI and more resolved than that of PMI, resembles the emission of the two separate chromophores. The individual contributions of the two chromophores to the lowest fluorescent singlet state of PDI-PMI cannot be resolved from the spectra, and in the remainder, we will simply designate the state as S_1. The absolute fluorescence quantum yield of PDI-PMI is rather high ($\Phi_F = 0.77$) in CHX but drops dramatically when going to TOL ($\Phi_F = 0.24$) or CB ($\Phi_F = 0.017$) (Figure 5 and Table 2). This drop in Φ_F in more polar solvents can be rationalized by the population of a nonfluorescent CT state ($PDI^{-\bullet}$-$PMI^{+\bullet}$, Figure 2a) from the S_1 state. Energetically, the $S_1 \rightarrow$CT electron transfer seems feasible because the energy of the S_1 state of $E(S_1)$ = ca. 2.3 eV (from the 0−0 emission) is larger than the difference between the oxidation and the reduction potential (1.95 eV), which is a first approximation for the energy of the CT state. With decreasing solvent polarity—the relative permittivity, ε_r, decreases in the order DCM, CB, TOL, CHX—E_{CT} is expected to increase, explaining why the CT state is not populated in CHX. A more accurate, experimental value for E_{CT} will be given in the next section.

The formation of the CT state may well be preceded by an energy transfer step between the PDI and the PMI chromophores. We consider, however, that it is virtually impossible to test this experimentally, because selective excitation of either chromophore in PDI-PMI is seriously hampered by their overlapping absorption spectra. In CHX, where CT formation is absent, we observe a single

TABLE 2: Absorption (λ_{abs}) and Fluorescence (λ_{em}) Maxima, Absolute Fluorescence Quantum Yields (Φ_F) Using C_{13}-PDI-C_{13} in $CHCl_3$ ($\Phi_F = 1.00$)[61] as a Reference, and Reconvolution Fits of the Photoluminescence Decay Traces at 535 nm at $T = 300$ K

solvent	λ_{abs} (nm)	λ_{em} (nm)	Φ_F	τ_1 (ns)	τ_2 (ps)	A_1/A_2	k_{rad} (ns^{-1})[a]
				PDI			
CHX	519	526	0.97	3.96			0.24
TOL	526	536	1.02	4.21			0.24
CB	529	538	0.96	4.34			0.22
				PMI			
CHX	485/513	533	0.85	3.65			0.23
TOL	492/519	550	0.87	3.85			0.23
CB	498/523	562	0.77	3.78			0.20
				PDI-PMI			
CHX	522	531	0.77	3.09			0.25
TOL	529	541	0.24	5.6	30 ± 10[b]	0.15 ± 0.05[b]	
CB	532	550	0.02	4.1 ± 0.1[c]	70 ± 10[b]	0.009 ± 0.002[b,c]	

[a] Radiative decay rate: $k_{rad} = \Phi_F/\tau_F$. [b] Because of the short τ_2 for PDI-PMI in TOL and the low A_1/A_2 in CB, these fits are less accurate; the error of τ_2 is linearly related to that of A_1/A_2 (e.g., if $\tau_2 = 20$ ps, $A_1/A_2 = 0.1$, and if $\tau_2 = 40$ ps, $A_1/A_2 = 0.2$). [c] In CB, the low PL quantum yield of PDI-PMI may cause τ_1 and A_1/A_2 to be less accurate.[49]

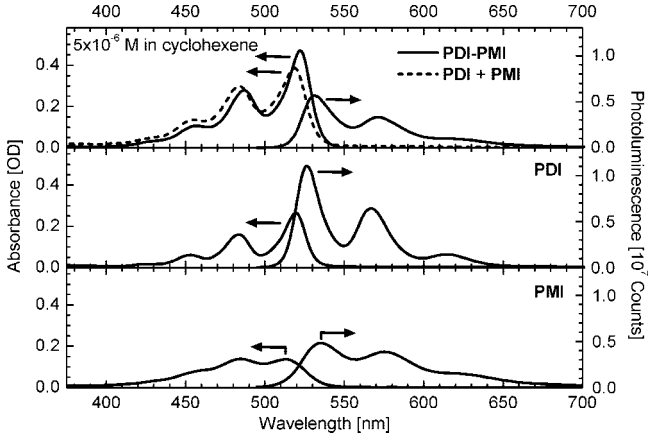

Figure 4. Absorbance (left axis) and fluorescence (right axis) spectra of PDI-PMI (top) and the reference compounds PDI and PMI (bottom) in CHX with the same concentration for all compounds (5×10^{-6} M). For the fluorescence spectrum of PDI-PMI, a 2× diluted sample was used. The emission spectra were corrected for the optical density (OD) at the excitation wavelength (485 nm), such that the relative intensities can be directly compared. The dashed line shows the sum of the absorption spectra of PDI and PMI.

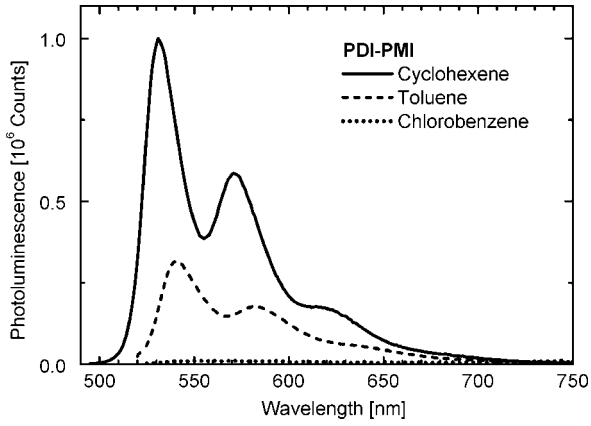

Figure 5. Fluorescence spectra of PDI-PMI in CHX, TOL, and CB.

decay time, which suggests that if energy transfer occurs, it will take place within a few picoseconds.

Electron Transfer Rates at $T = 300$ K. Upon photoexcitation, the fluorescence of the PDI and PMI reference compounds decays monoexponentially, and fluorescence lifetimes

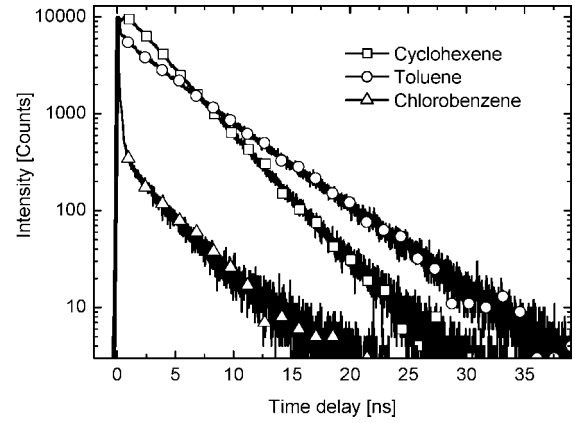

Figure 6. Time-resolved photoluminescence traces of PDI-PMI in different solvents. Excited at 400 nm, and the emission was detected at 535 nm.

of $\tau = 3.75 \pm 0.1$ ns for PMI and $\tau = 4.15 \pm 0.2$ ns for PDI were obtained in CHX, TOL, and CB (Table 2). For PDI-PMI, the traces are strongly solvent-dependent: In CHX, the emission decays monoexponentially ($\tau = 3.09$ ns), while in TOL and CB the traces show a distinct biexponential decay with a slow (τ_1) and a fast (τ_2) component (Figure 6 and Table 2). This can be explained by the absence (in CHX) and presence (in the other two solvents) of a dynamic equilibrium between the emissive S_1 state and the nonemissive CT state (Figure 2a). In the dynamic equilibrium, forward electron transfer ($S_1 \rightarrow CT$) is followed by a back electron transfer reaction, repopulating the singlet excited state ($CT \rightarrow S_1$).

For PDI-PMI in CHX, we assume that electron transfer is absent ($k_{ET} \approx 0$), because Φ_F is high and because the fluorescence intensity decays monoexponentially with a lifetime that is similar to those of the individual chromophores. The rates of fluorescence (k_F) and nonradiative decay (k_{NR}) can then be determined from τ and Φ_F (from steady state fluorescence) according to

$$\frac{1}{\tau} = k_F + k_{NR} \tag{2}$$

$$\Phi_F = \frac{k_F}{k_F + k_{NR}} \tag{3}$$

By substituting $\Phi_F = 0.77$ and $\tau = 3.09$ ns, we find $k_F = 0.25$ ns^{-1} and $k_{NR} = 0.076$ ns^{-1} in CHX (Table 3).

TABLE 3: Electron Transfer Rates at $T = 300$ K for PDI-PMI in Various Solvents from Analysis of Fluorescence and ps-PIA Decay Traces

method	solvent	k_F (ns^{-1})	k_{NR} (ns^{-1})	k_{ET} (ns^{-1})	k_{BET} (ns^{-1})	k_{CR} (ns^{-1})	Φ_F[a]	Φ_F (ST)[b]
TR-PL	CHX	0.25	0.076					0.77
TR-PL	TOL[c]	0.25	0.076	30 ± 10	4.0 ± 0.5	0.16 ± 0.01	0.20 ± 0.06	0.24
TR-PL	CB[c,d]	0.25	0.076	14 ± 2	0.05 ± 0.01	0.24 ± 0.01	0.021 ± 0.004	0.017
ps-PIA	TOL	0.25	0.076	21 ± 4	4.6 ± 2	0.1 ± 0.3		
ps-PIA	CB	0.25	0.076	13 ± 3	<1.4	0.5 ± 0.2		

[a] From eq 10. [b] From steady-state PL. [c] The uncertainty in the fits of the short component in CB and TOL results in the tabulated uncertainties for the transfer rates (relatively large for k_{ET} in TOL) and Φ_F. [d] The low PL quantum yield of PDI-PMI in CB at $T = 300$ K causes k_{BET} and k_{CR} to be less accurate than in TOL.[49]

For PDI-PMI in TOL and CB, k_{ET}, k_{BET}, and k_{CR} (Figure 2a) can be determined from the fluorescence lifetime measurements in combination with a kinetic model that includes both forward electron transfer and back electron transfer to S_1. The concentration of S_1 states ($[S_1]$) is related to the rate constants according to[38c,62]

$$[S_1] = [S_1]_0\left(\frac{A_1}{A_1+A_2}e^{-t/\tau_1} + \frac{A_2}{A_1+A_2}e^{-t/\tau_2}\right) \quad (4)$$

with $[S_1]_0$ the concentration of singlet excited states at $t = 0$ and

$$A_1 = \frac{\tau_2^{-1} - k_F - k_{NR} - k_{ET}}{\tau_2^{-1} - \tau_1^{-1}} \quad (5)$$

$$A_2 = \frac{k_F + k_{NR} + k_{ET} - \tau_1^{-1}}{\tau_2^{-1} - \tau_1^{-1}} \quad (6)$$

$$\frac{1}{\tau_{1,2}} = \frac{1}{2}\left(k_F + k_{NR} + k_{ET} + k_{BET} + k_{CR} \mp \sqrt{(k_{BET} + k_{CR} - k_F - k_{NR} - k_{ET})^2 + 4k_{ET}k_{BET}}\right) \quad (7, 8)$$

The fluorescence of PDI-PMI is linearly dependent on the concentration of singlet excited states ($I_F \propto [S_1]$). Analysis of the PL decay traces in TOL and CB provides A_1 and A_2 and the two decay times τ_1 and τ_2 according to eq 4. For the reference compounds PDI and PMI, only a minor solvent dependence is found for τ (3.75 ± 0.10 ns for PMI and 4.15 ± 0.20 ns for PDI) and Φ_F (0.82 ± 0.05 for PMI and 0.98 ± 0.02 for PDI); thus, we can assume that k_{NR} and k_F of the dimer are also only weakly solvent-dependent. Then, the forward electron transfer rate (k_{ET}) can be obtained using k_F and k_{NR} from PDI-PMI in CHX and after rewriting eqs 5 and 6:

$$k_{ET} = \frac{A_1\tau_1^{-1} + A_2\tau_2^{-1}}{A_1 + A_2} - k_F - k_{NR} \quad (9)$$

Subsequently, k_{BET} and k_{CR} can be obtained from eqs 7, 8. The electron transfer rates (k_{ET}, k_{BET}, and k_{CR}) for PDI-PMI in TOL and CB following this analysis are given in Table 3.

Additionally, from these rates, the fluorescence quantum yield can be calculated

$$\Phi_F = \frac{k_F(k_{BET} + k_{CR})}{(k_F + k_{NR})(k_{BET} + k_{CR}) + k_{ET}k_{CR}} \quad (10)$$

The fluorescence quantum yields obtained from the time-resolved measurements (Table 3) are in excellent agreement with those independently determined by steady state fluorescence, showing the validity of the approach. However, because of the fast k_{ET}, the accuracy of the measurement in TOL is limited due to the time response of the TR-PL setup.

An alternative technique to study electron transfer processes is via ps-PIA, by which ground state bleaching, PIA of charged species, as well as luminescence signals can be probed. Time traces at $\lambda_{probe} = 540$ and 955 nm ($\lambda_{pump} = 490$ nm) are shown for TOL (Figure 7a) and CB (Figure 7b). The CT state absorption is assumed to be characterized by a complementary absorption of the radical cation of PMI and the radical anion of PDI.[38c,45,63] Thus, at 540 nm, the emission from the S_1 state (positive $\Delta T/T$) and the absorption of the CT state (negative $\Delta T/T$) are probed, while at 955 nm the $\Delta T/T$ signal is the sum of $S_1 - S_n$ and $CT_1 - CT_n$ absorption. This yields the following equations:

$$\Delta T/T\,(540\text{ nm}) = -c_1[S_1] + c_2[CT] \quad (11)$$

$$\Delta T/T\,(955\text{ nm}) = c_3[S_1] + c_4[CT] \quad (12)$$

where c_1–c_4 are positive scaling factors related to the fluorescence intensity (c_1) or the extinction coefficients (c_2–c_4) of the chemical species at the probe wavelengths. Note that the sign of the scaling factors is indicated in eqs 11 and 12. $[S_1]$ is described by eq 4, and the concentration CT states ([CT]) are described by eq 13:[38c,62]

$$[CT] = [S_1]_0A_3(e^{-t/\tau_1} - e^{-t/\tau_2}) \quad (13)$$

$$A_3 = \frac{k_{ET}}{\tau_2^{-1} - \tau_1^{-1}} \quad (14)$$

Thus eqs 11 and 12 describe the signal intensity as a function of k_F, k_{NR}, k_{ET}, k_{BET}, and k_{CR}, and the coefficients c_1–c_4. By a simultaneous analysis of both wavelength traces and by using k_F and k_{NR} from the fluorescence in CHX, k_{ET}, k_{BET}, and k_{CR} are obtained in TOL and CB (Table 3). Most values are within experimental error from those acquired by the fluorescence measurements and that of k_{ET} in TOL is more accurately determined via PIA. Only for k_{CR} in CB is a higher value found than by fluorescence. The low Φ_F of PDI-PMI in CB at $T = 300$ K can explain why the determination of k_{CR} by ps-PIA is more accurate than by fluorescence methods.

To summarize the measured transfer rates using time-resolved fluorescence and ps-PIA at $T = 300$ K, we suppose that k_{ET} is absent in CHX, while in TOL fast electron transfer (k_{ET} = ca. 25 ns^{-1}) and back electron transfer (k_{BET} = ca. 4 ns^{-1}) occurs. In CB, electron transfer and back transfer are slower by 40% (k_{ET} = ca. 15 ns^{-1}) and a factor of 80 (k_{BET} = ca. 0.05 ns^{-1}), respectively. The charge recombination rate in TOL (k_{CR} = ca. 0.16 ns^{-1}) is about 150× slower than k_{ET}, while in CB (k_{CR} = ca. 0.5 ns^{-1}), it is about 30× slower than k_{ET} in the same solvent.

Having established both k_{ET} and k_{BET}, we can directly determine the Gibb's free energy of electron transfer (ΔG_{ET}) via

$$\Delta G_{ET} = -k_B T \ln\left(\frac{k_{ET}}{k_{BET}}\right) \quad (15)$$

We find that in TOL and CB, ΔG_{ET} amounts to about −50 and −150 meV, respectively. It is of interest to establish the ΔG_{ET} that makes electron transfer quantitative. For this, we have determined k_{ET} and k_{BET} in TOL:CB solvent mixtures at 300 K (Figure 8). At a 1:1 ratio of TOL and CB, k_{BET} drops below $k_{ET}/100$. From this, we conclude that a charge separation (over 14 Å), without significant back electron transfer, can be achieved with a relatively low driving force for electron transfer of only $\Delta G_{ET} = -120$ meV. Under these conditions, we can ignore k_{BET} as compared to k_{ET} and calculate the quantum yield for electron transfer from $\Phi_{ET} = k_{ET}/(k_{ET} + k_F + k_{NR}) = 98\%$. This demonstrates that near quantitative electron transfer can be obtained for a driving force as low as −120 meV. We note that the equilibrium that exists between S_1 and CT allows us to determine both k_{ET} and k_{BET} and, hence, an accurate experimental determination of ΔG_{ET}, from which E_{CT} can be determined via $E_{CT} = E(S_1) + \Delta G_{ET}$.

Temperature Dependence of CT Kinetics. After obtaining the electron transfer rates (k_{ET}, k_{BET}, and k_{CR}) at $T = 300$ K, the barriers for these processes can be obtained from temperature-dependent measurements. The fluorescence decay traces distinctly change with temperature. The short component (τ_1) in the time traces becomes much more important upon cooling a PDI-PMI solution in TOL from $T = 300$ to 220 K (Figure 9a and Supporting Information, Table S2). After analysis, we find that the lower temperature causes a reduction of k_{ET} and k_{BET} with a factor of 2 (from $k_{ET} = 40 \pm 10$ to 15 ns^{-1}) and with 2 orders of magnitude (from $k_{BET} = 4 \pm 0.5$ to 0.03 ns^{-1}), respectively, while k_{CR} (= 0.18−0.16 ns^{-1}) remains virtually constant between $T = 300$ and 220 K (Table S2 of the Supporting Information). Note that at $T = 300$ K, we actually find a faster rate than obtained in the previous section ($k_{ET} = 30 \pm 10$ ns^{-1}, Table 3). This difference indicates the inaccuracy caused by the short decay time that is near the response time of TR-PL setup at $T = 300$ K. At lower temperature, the short decay time increases and the measurements improve in accuracy.

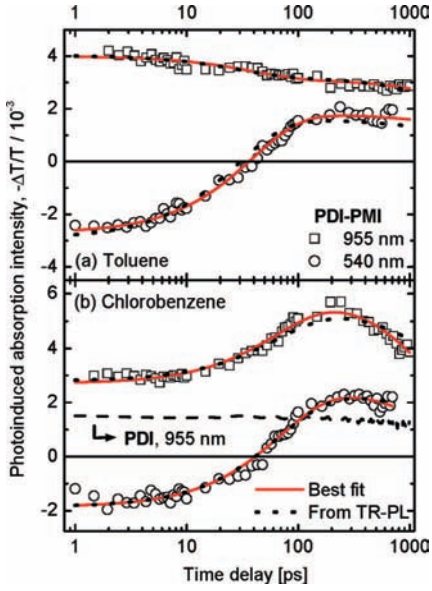

Figure 7. ps-PIA traces of PDI-PMI in TOL (a) and CB (b). Pump, $\lambda_{pump} = 490$ nm; and probe, $\lambda_{probe} = 540$ nm (○) or $\lambda_{probe} = 955$ nm (□). In panel b, the ps-PIA trace of PDI in CB (dashed line) is also shown. The solid lines are best fits through the data using eqs 11 and 12, and the dotted lines give the best fit if the rates obtained by fluorescence are used as input parameters.

By using Eyring's formula:

$$k_0 = \frac{k_B T}{h} \exp\left(\frac{\Delta S_0^{\#}}{k_B}\right) \exp\left(-\frac{\Delta H_0^{\#}}{k_B T}\right) \quad (16)$$

and plotting $k_B \ln(hk_0/k_B T)$ vs T^{-1} (Figure 9b, top) the changes in enthalpy (the slope gives $-\Delta H_0^{\#}$) and entropy (the intercept with the ordinate gives $\Delta S_0^{\#}$) for the electron transfer and back transfer and charge recombination process are obtained (Table S3 of the Supporting Information). From these, ΔG_{ET} and the heights of the barriers (from $\Delta G_0 = \Delta H_0 - T\Delta S_0$) for the three processes are found at each temperature (Figure 10a for $T = 220$ and 300 K).

The same results follow from eq 15: ΔG_{ET} is enhanced with a lowering of the temperature (from ΔG_{ET} = ca. −50 meV at $T = 300$ K to −120 meV at $T = 220$ K). The temperature dependence of ΔG_{ET} is given in Figure 9c together with Φ_F (from eq 10), which decreases with 1 order of magnitude upon going from $T = 300$ to 220 K.

Also in CB, the rates for electron transfer and back transfer are temperature-dependent; however, the effects are less dramatic than in TOL: There is a mere 35% increase of k_{ET} upon going from $T = 300$ to 380 K, while k_{BET} increases by a factor of ∼4 and k_{CR} increases by less than 25% between $T = 340$ and 380 K (Table S2 of the Supporting Information and Figure 9b, bottom). High temperature measurements were carried out in contrast to TOL, because in CB the fits become better upon *increasing* the temperature, the limiting factor at lower temperature being the low Φ_F.

Using Eyring's formula (eq 16), we can again calculate the overall change in enthalpy and entropy for electron transfer and the barriers for the electron transfer and back transfer and charge recombination (Figure 9b and Table S3 of the Supporting Information). The heights of the barriers in CB are depicted in Figure 10b for $T = 300$ and 380 K, along with the energies (E_{CT}) of the CT state relative to the S_1 state. The fluorescence quantum yield increases from $\Phi_F = 0.02$ at 340 K to $\Phi_F = 0.03$ at 380 K, while ΔG_{ET} increases with temperature from $\Delta G_{ET} = -0.13$ to −0.11 eV between $T = 340$ and 380 K (Table S2 of the Supporting Information and Figure 9c).

The more negative value of ΔG_{ET} (and correspondingly higher $\Delta G_{BET}^{\#}$) explains why k_{BET} is much slower in CB than in TOL, causing a 10× lower Φ_F in CB, even with the higher k_{ET} in TOL. With increasing temperature, we find that for both solvents $\Delta G_{ET}^{\#}$ and $\Delta G_{CR}^{\#}$ increase along with the energy of the CT state (E_{CT}), while $\Delta G_{BET}^{\#}$ decreases. Note that while $\Delta G_{ET}^{\#}$ and $\Delta G_{CR}^{\#}$ increase with temperature, the higher Boltzmann energy ($k_B T = 19$, 26, and 33 meV at $T = 220$, 300, and 380 K, respectively)

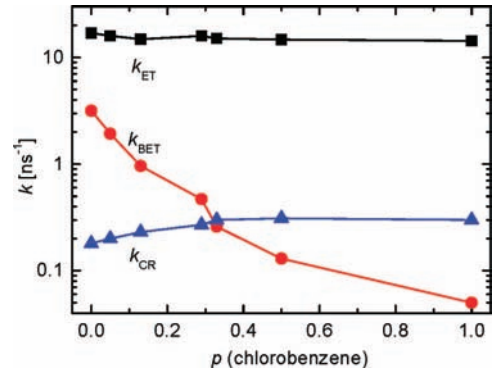

Figure 8. k_{ET}, k_{BET}, and k_{CR} determined by TR-PL at $T = 300$ K vs the fraction (p) of CB for a TOL/CB solution containing a constant concentration of PDI-PMI.

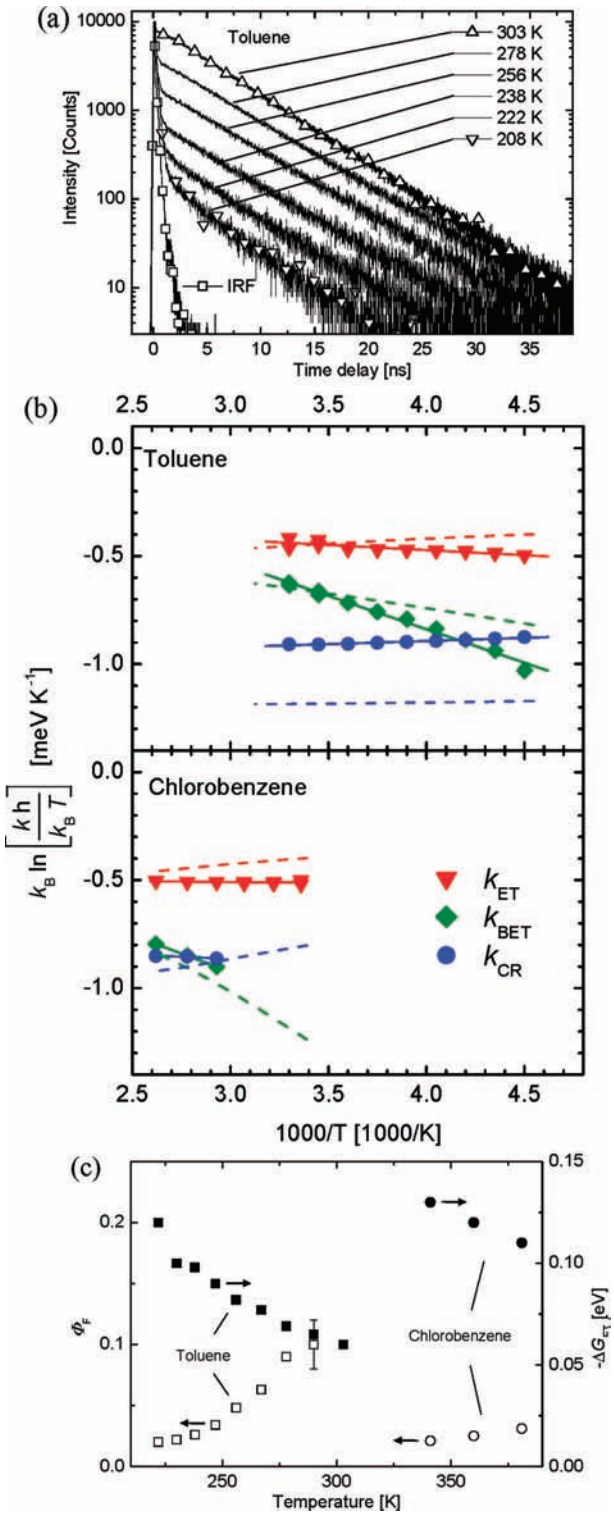

Figure 9. (a) Temperature dependence of time-resolved photoluminescence of PDI-PMI in TOL. The solution was excited at $\lambda_{exc} = 400$ nm, and the emission was detected at $\lambda_{em} = 540$ nm. (b) Plots of $k_B \ln(hk_0/k_BT)$ with $k_0 = k_{ET}$, k_{BET}, and k_{CR} vs $1/T$ for PDI-PMI in TOL for $T = 220-300$ K (top) and in CB for 300−380 K (bottom) from photoluminescence decay analysis. The solid lines are linear fits through the data. The intercepts and slopes of these fits give $\Delta S_0^{\#}$ and $\Delta H_0^{\#}$, respectively. The dashed lines are predictions using Marcus−Jortner. For ϵ_r and n, see the Supporting Information). For TOL, the apparent ϵ_{app} is used. (c) Temperature-dependent fluorescence quantum yield (left axis) and driving force for electron transfer (right axis) for PDI-PMI in TOL (open symbols) and CB (closed symbols), derived from time-resolved fluorescence using eqs 10 and 15. At $T < 230$ K for TOL and at $T < 340$ K for CB, the low Φ_F causes k_{BET} to be less accurate.[49] At $T \geq 290$ K for TOL, the low value of τ_2 affects the accuracy of determining k_{ET} and k_{BET} as indicated by the error bar for Φ_F.

still makes k_{ET} and k_{CR} faster at higher temperature. It is remarkable that at $T = 300$ K the barrier for forward electron transfer ($\Delta G_{ET}^{\#}$) is 20 meV lower in TOL than in CB, despite a 110 meV lower ΔG_{ET} in CB.

Population of the Triplet Excited State at $T = 300$ K. After the analysis of the rates and barriers for electron transfer, back transfer, and charge recombination, we will now focus on the formation of triplet excited states that are formed after photoexcitation. With ns-PIA, we observe that triplet excited states are populated after formation of the PDI-PMI CT state. Photoexcitation of PDI-PMI in N_2-saturated TOL at 488 nm leads to a PIA spectrum that is typical for the T_1-T_n absorption of PDI (Figure 11),[44] with its absorption in the same spectral region as the bleaching bands. The rise of the signal intensity is faster (<50 ns) than the time response of the setup, while the triplet lifetime is $\tau_T = 14 \pm 2$ μs. In CB, a similar T_1-T_n absorption is observed with $\tau_T = 5 \pm 1$ μs, whereas in CHX no PIA signal could be detected, indicating a much lower triplet quantum yield (Φ_T) in this solvent. Also, for PDI in CB, no T_1-T_n absorption could be detected. Upon addition of oxygen, the decay time of the PDI-PMI triplets in TOL as well as in CB was reduced by more than a factor of 10. PDIs have a lowest triplet excited state energy of $E(T_1) = 1.20$ eV,[44] and for PDI-PMI, we expect a similar $E(T_1)$ because of the similar $E(S_1)$ of the molecules. The triplet quenching by oxygen is in agreement with this expectation, allowing the population of the singlet oxygen ($^1\Delta_g$) state with an energy of 0.98 eV above its triplet ground state ($^3\Sigma_g^-$).[64]

The triplet quantum yield (Φ_T) of PDI-PMI can be determined from singlet oxygen ($^1\Delta_g$) luminescence measurements via the relation: $\Phi_\Delta = \Phi_T f_T S_\Delta$, in which Φ_Δ is the singlet oxygen ($^1\Delta_g$) quantum yield, f_T is the fraction of triplet states trapped by oxygen in a given system, and S_Δ is the efficiency of singlet oxygen ($^1\Delta_g$) generation from the quenched triplet state. From the strong reduction of τ_T upon the addition of oxygen, we infer that f_T is close to unity for PDI-PMI in oxygen-saturated TOL and CB. S_Δ of $\pi-\pi^*$-excited triplet states of aromatic hydrocarbons are generally also close to unity ($S_\Delta = 0.8-1.0$), especially if $E(T_1)$ is close to the energy of singlet oxygen ($^1\Delta_g$).[64] Thus, although Φ_Δ gives a lower limit, it approximates the actual value of Φ_T.

Singlet oxygen ($^1\Delta_g$) quantum yields (Φ_Δ) were determined for PDI-PMI in benzene (BZ), CHX, TOL, and CB by excitation at 532 nm and probing the oxygen ($^1\Delta_g$) phosphorescence decay as described in the Experimental Section. Φ_Δ provides lower limits for Φ_T, revealing $\Phi_T^{CHX} \geq 0.10 \pm 0.08$, $\Phi_T^{BZ} \geq 0.57 \pm 0.14$, $\Phi_T^{TOL} \geq 0.56 \pm 0.14$, and $\Phi_T^{CB} \geq 0.42 \pm 0.11$ (Table 4). In all solvents, Φ_T is consistent with the measured fluorescence quantum yield ($\Phi_F + \Phi_T \leq 1$). The lower limits for Φ_T^{TOL} and Φ_T^{CB} are larger than the upper limit for Φ_T^{CHX} determined from the fluorescence quantum yield ($\Phi_T \leq 1 - \Phi_F = 0.23$). This indicates that ISC from ^{1}CT to T_1 (in TOL and CB) is more efficient than ISC from S_1 to T_1 (in CHX).

ISC Rates. The decay pathways of photoexcited PDI-PMI can be described by quantum yields from the S_1 and the CT state, the sum of which is unity. These quantum yields are those of fluorescence (Φ_F, radiative decay to S_0), triplet formation (Φ_{Ti}, ISC to T_1), and nonradiative decay (Φ_{NRi}, internal conversion to S_0). The subscript $i = 1$ denotes decay directly from S_1 and $i = 2$ denotes decay via the CT state (to T_1 or S_0). Radiative decay from the CT state is not observed ($\Phi_{F,CT} \ll 0.01$) and is neglected in this analysis. The corresponding labeling of transfer rates is depicted in Figure 2b.

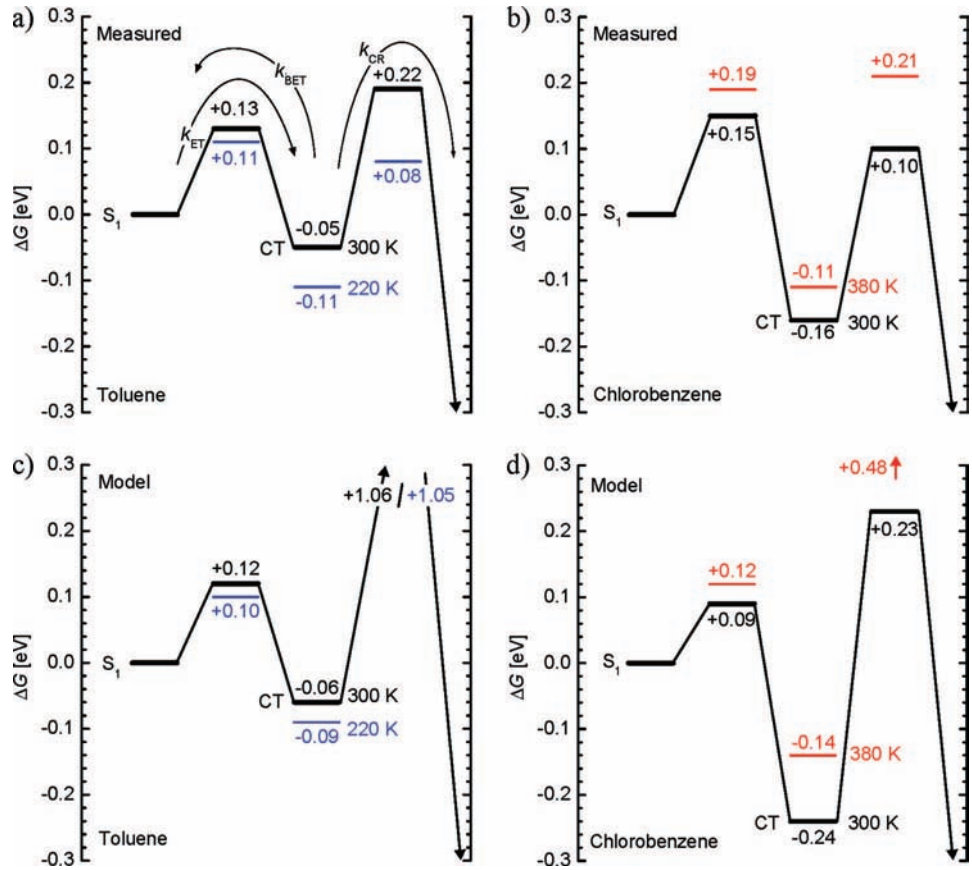

Figure 10. Schematic of the barriers (in free energy) for electron transfer, back-transfer, and charge recombination at $T = 220$ (separated lines) and 300 K (connected lines) in TOL (a and c) and $T = 300$ (connected lines) and 380 K (separated lines) in CB (b and d), as determined from temperature-dependent time-resolved fluorescence (a and b) and from the Marcus−Jortner model (c and d).

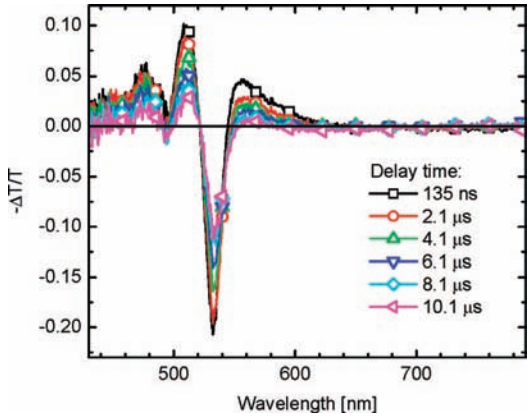

Figure 11. ns-PIA spectra of PDI-PMI in N_2-saturated TOL, using an excitation wavelength of $\lambda_{exc} = 488$ nm (5 ns width, 35 μJ) and the indicated delay times.

The ranges for Φ_{Ti}^{Sol} and Φ_{NRi}^{Sol} can be determined using Φ_F^{Sol} and Φ_Δ^{Sol} in each solvent (Sol), from

$$\Phi_F^{Sol} + \Phi_{T1}^{Sol} + \Phi_{NR1}^{Sol} + \Phi_{T2}^{Sol} + \Phi_{NR2}^{Sol} = 1 \quad (17)$$

$$\Phi_{T1}^{Sol} + \Phi_{T2}^{Sol} \geq \Phi_\Delta^{Sol} \quad (18)$$

For CHX, Φ_{T2}^{CHX} and Φ_{NR2}^{CHX} are 0, because the CT state is not populated. The lower limit for the triplet yield from the S_1 state follows from eq 18 by recalling that $\Phi_{T1}^{CHX} \geq \Phi_\Delta^{CHX} = 0.10 \pm 0.08$, while the upper limit follows from eq 17 by $\Phi_{T1}^{CHX} \leq 1 - \Phi_F^{CHX} = 0.23$. The upper limit for Φ_{NR1}^{CHX} then also follows by $\Phi_{NR1}^{CHX} = 1 - \Phi_F^{CHX} - \Phi_{T1}^{CHX} \leq 0.21$ (Table 4).

If we assume again that k_{NR} ($= k_{NR1} + k_{T1}$) and k_F of PDI-PMI are solvent-independent, $\Phi_{T1}^{Sol} + \Phi_{NR1}^{Sol}$ is obtained for the other solvents:

$$\Phi_{T1}^{Sol} + \Phi_{NR1}^{Sol} = \frac{\Phi_F^{Sol}(\Phi_{T1}^{CHX} + \Phi_{NR1}^{CHX})}{\Phi_F^{CHX}} \quad (19)$$

Because of the fast deactivation of the S_1 state and correspondingly low PL yields, this also results in low values: $\Phi_{T1}^{TOL} + \Phi_{NR1}^{TOL} = 0.07$ and $\Phi_{T1}^{CB} + \Phi_{NR1}^{CB} = 0.005$, which are the upper limits for Φ_{T1} and Φ_{NR1}. Subsequently, the lower limit for Φ_{T2}^{Sol} is obtained by substituting the upper limit for Φ_{T1}^{Sol} in eq 18, yielding $\Phi_{T2}^{TOL} \geq 0.35$ and $\Phi_{T2}^{CB} \geq 0.31$. Finally, the upper limits for Φ_{T2}^{Sol} and Φ_{NR2}^{Sol} are determined by eq 17. The quantum yields PDI-PMI in CHX, TOL, and CB are summarized in Table 4.

From Φ_{T1} in CHX and the measured decay time ($\tau = 3.09$ ns, Table 2), the ISC rate from the S_1 state is obtained as follows: $k_{T1}^{CHX} = \Phi_{T1}/\tau = 0.006-0.074$ ns^{-1}. From k_{CR} ($=k_{T2} + k_{NR2}$, Table 3), Φ_{T2}, and Φ_{NR2}, the decay rates from the CT state (k_{T2} and k_{NR2}) are determined for TOL and CB, using

$$k_{T2}^{Sol} = \frac{\Phi_{T2}^{Sol}}{\Phi_{T2}^{Sol} + \Phi_{NR2}^{Sol}} k_{CR}^{Sol} \quad (20)$$

$$k_{NR2}^{Sol} = \left(1 - \frac{\Phi_{T2}^{Sol}}{\Phi_{T2}^{Sol} + \Phi_{NR2}^{Sol}}\right) k_{CR}^{Sol} \quad (21)$$

The rates for k_{T2}^{TOL} and k_{T2}^{CB} are 0.075−0.17 and 0.1−0.7 ns^{-1}, respectively, and are significantly faster than k_{T1}^{CHX}. Note that although Φ_Δ^{TOL} is higher than Φ_Δ^{CB}, k_{T2}^{CB} may be higher than

TABLE 4: Measured Quantum Yields of Singlet Oxygen ($^1\Delta_g$) Luminescence (Φ_Δ), PDI-PMI Fluorescence (Φ_F), Triplet Formation (Φ_T), and Nonradiative Decay (Φ_{NR}) and the Rates (k_{T2} and k_{NR2}) Obtained from These in Air-Saturated Solvents at $T = 300$ K as Compared to Predictions by Marcus−Jortner Theory Using $V_{S1\text{-}CT} = V_{CT\text{-}S0} = 6$ meV and $V_{CT\text{-}T1} = 0.17$ meV

	measured			predicted	
solvent	CHX	TOL	CB	TOL	CB
Φ_Δ	0.02−0.18[a]	0.42−0.70	0.31−0.52		
Φ_F	0.77[b]	0.24[b]	0.017[b]	0.12	0.004
$\Phi_{T1} + \Phi_{NR1}$	0.23[c]	0.07[d]	0.005[d]	0.04	0.001
$\Phi_{T2} + \Phi_{NR2}$	0	0.69[c]	0.98[c]	0.85	0.99
Φ_{T1}	0.02−0.23[d,d]	0−0.07[d]	0−0.005[d]		
Φ_{NR1}	0−0.21[d]	0−0.07[d]	0−0.005[d]		
Φ_{T2}	0	0.35−0.69[c,e]	0.31−0.98[c,e]	0.80	0.25
Φ_{NR2}	0	0−0.34[c]	0−0.67[c]	0.05	0.74
k_{CR} (ns^{-1})[f]		0.15−0.17	0.3−0.7		
k_{T2} (ns^{-1})		0.075−0.17[g]	0.1−0.7[g]	0.12	0.17
k_{NR2} (ns^{-1})		0−0.085[h]	0−0.5[h]	0.008	0.51

[a] Extrapolation to $t = 0$ results in a significant error because τ_Δ is shorter and because I_P^0 is lower. [b] From Table 2. [c] From eq 17. [d] From eq 19. [e] Lower limit from eq 18. [f] From Table 3. [g] From eq 20. [h] From eq 21.

k_{T2}^{TOL}. First, the higher Φ_Δ^{TOL} may partially be caused by the longer triplet lifetime measured in N_2-saturated TOL ($\tau_T^{TOL} = 14$ μs vs $\tau_T^{CB} = 5$ μs), causing an enhanced triplet trapping efficiency (f_T). Second, the decay rate from CT to S_0 (k_{NR2}) is likely much lower in TOL, which would lead to a high Φ_T^{TOL}, even for a slow k_{T2}^{TOL}.

Prediction of the Gibb's Free Energy for Electron Transfer. The experimentally obtained rates and barriers for the electron transfer processes depicted in Figure 2b will be compared to an electronic model based on Marcus−Jortner theory. The semiquantitative model described by Weller can be used to estimate the Gibb's free energy (ΔG_{ET}) for electron transfer on the basis of the relative permittivity (ε_r) of the solvent:[4b]

$$\Delta G_{ET} = e[E^\circ(D/D^+) - E^\circ(A/A^-)] - E(S_1) - \frac{e^2}{4\pi\varepsilon_0\varepsilon_r R_{CC}} - \frac{e^2}{8\pi\varepsilon_0}\left(\frac{1}{r^+} + \frac{1}{r^-}\right)\left(\frac{1}{\varepsilon_{ref}} - \frac{1}{\varepsilon_r}\right) \quad (22)$$

in which $E(S_1)$ is the energy of the lowest singlet excited state, e and ε_0 are the elementary charge and the vacuum permittivity, $E^\circ(D/D^+)$ and $E^\circ(A/A^-)$ are the redox potentials of the electron donating and accepting part of the molecule measured in a solvent with relative permittivity ε_{ref}, R_{CC} is the center-to-center distance of the two charges, and r^+ and r^- are the radii of the positively and negatively charged species.

The results obtained from eq 22 are given in Table 5 for PDI-PMI in CHX, TOL, and CB at $T = 300$ K using the following parameters: a solvent-dependent $E(S_1)$, from the emission maximum of PMI, $E^\circ(D/D^+) = +0.915$ V and $E^\circ(A/A^-) = -1.040$ V vs Fc/Fc^+ in DCM (Table 1), $r^+ = r^- = 4.7$ Å,[40] and $R_{CC} = 14$ Å (based on molecular modeling).

The results correspond to the observations that forward electron transfer takes place in CB (where $\Delta G_{ET} = -0.24$ eV), while it does not in the less polar CHX (where $\Delta G_{ET} = +0.21$ eV). However, the positive value found for TOL ($\Delta G_{ET} = +0.22$ eV) contradicts the experimental results by indicating that electron transfer should not take place.

TABLE 5: Results of Eq 22, Using $E^\circ(D/D^+) = +0.915$ V and $E^\circ(A/A^-) = -1.040$ V, $r^+ = r^- = 4.7$ Å, $R_{CC} = 14$ Å, and the Value of ε_r at $T = 300$ K

solvent	$E(S_1)$ (eV)[a]	E_{CT} (eV)[b]	ΔG_{ET} (eV)
CHX	2.33	2.54	+0.21
TOL	2.25	2.47	+0.22
TOL[c]	2.25	2.19	−0.06
CB	2.21	1.97	−0.24

[a] From $\lambda_{max,em}$ of PMI. [b] $E_{CT} = E(S_1) + \Delta G_{ET}$. [c] Here, an "apparent ε_r" is used (see the text and Table S4 of the Supporting Information).

Solvents like TOL and dioxane (DIOX) are special because they often show larger stabilization energies of states with CT character, leading to a further red shift of the CT type emission than predicted from their "bulk" relative permittivity: $\varepsilon_r = 2.27$ for dioxane and $\varepsilon_r = 2.37$ for TOL. These anomalies are well-known for solvents that have a low dipole moment but a high quadrupole moment; this class of solvents is referred to as nondipolar solvents to distinguish them from low-dielectric nonpolar solvents such as alkanes.[65] Reichardt's polarity (E_T^N, Table S4 of the Supporting Information)[66] scale is derived from the Stokes' shift of a betaine probe. For PDI-PMI, we observe a strong correlation between the E_T^N of the solvent and the amount of PL quenching (Figure 12a). Because ε_r does not give a good description of the solvent−molecule interactions, a so-called "apparent dielectric permittivity" (ε_{app}) was introduced, such that the nondipolar solvent under consideration behaves as a hypothetical dipolar solvent of polarity ε_{app}.[67−70] From the relation between ε_r and E_T^N (Figure 12b), values of $\varepsilon_{app} = 3.5$ and 5.2 are found for TOL and DIOX, respectively. The value for DIOX is similar to that calculated ($\varepsilon_{app} = 6.4-7.7$),[69] and experimentally obtained ($\varepsilon_{app} = 6.5$)[71] for smaller solutes.[72] For TOL, $\varepsilon_{app} = 4.3$ was calculated for a solute with a radius of 4.3 Å.[70] Hence, $\varepsilon_{app} = 3.5$ ($=\varepsilon_r + 1.15$) for TOL seems a reasonable value for PDI-PMI.

The effect of replacing ε_r by ε_{app} in eq 22 makes that the calculated value of ΔG_{ET} changes from $\Delta G_{ET} = +0.22$ eV to $\Delta G_{ET} = -0.06$ eV (Table 5), which compares better to the observed PL quenching. If temperature-dependent values for ε_r[77] are used, eq 22 gives a good description of the lower driving force for electron transfer (less negative ΔG_{ET}) at higher temperature, caused by a reduction of ε_r. For TOL, the calculated values correspond within 0.02 eV to those obtained from the photoluminescence measurements, if an apparent relative permittivity [$\varepsilon_{app} = \varepsilon_r(T) + 1.15$] is used (viz. Figure 10a,c). For CB, the predicted value is off by 0.08 eV at $T = 300$ K and by only 0.03 eV at $T = 380$ K. The better prediction at higher temperature ($T > 340$ K) could be partially explained by the higher accuracy in the determination of k_{BET} due to the higher PL quantum yield.[49]

Marcus−Jortner Model. The experimental energy barriers can be compared to those obtained from the Marcus equation:[73]

$$\Delta G_0^{\#} = \frac{(\Delta G_0 + \lambda)^2}{4\lambda} \quad (23)$$

Here, λ represents the reorganization energy, being the sum of the internal (λ_i) and solvent (λ_s) reorganization energies. The internal reorganization energy was set to $\lambda_i = 0.25$ eV, a value typical for large aromatics,[74] and following previous studies on PDIs.[38b,45] The solvent contribution can be estimated using the Born−Hush approach, in which n is the refractive index of the solvent:[75]

$$\lambda_s = \frac{e^2}{4\pi\varepsilon_0}\left[\frac{1}{2}\left(\frac{1}{r^+}+\frac{1}{r^-}\right)-\frac{1}{R_{CC}}\right]\left(\frac{1}{n^2}-\frac{1}{\varepsilon_r}\right) \quad (24)$$

The rates for electron transfer, back transfer, and charge recombination can then be predicted by the semiclassical Marcus expression,[73] adapted by Jortner, who introduced higher vibrational levels:[74,76]

$$k_0 = \left(\frac{4\pi^3}{h^2\lambda_s k_B T}\right)^{1/2} V^2 e^{-S}\sum_{n=0}^{\infty}\left[\frac{S^n}{n!}\exp\left(-\frac{(\Delta G_0+\lambda_s+nh\nu)^2}{4\lambda_s k_B T}\right)\right] \quad (25)$$

Here, S ($=\lambda_i/h\nu$) relates to the effective mode vibrational energy. We have used a value of 0.186 eV ($=1500$ cm^{-1}) for $h\nu$, a typical value representing the stretch vibration of the carbon−carbon double bond in aromatic systems.[38b,45,74] V describes the electronic coupling of the two states involved in the CT reaction. For the transition from S_1 to ^{1}CT, ΔG_0 equals ΔG_{ET} or $-\Delta G_{ET}$ for k_{ET} and k_{BET}, respectively. We obtain V_{S_1}−CT = 5−7 and 7−8 meV, respectively, from k_{ET} and k_{BET} measured in TOL at $T = 300$ K. These values are similar to that of 2.4 meV reported for a PDI-phenyl-PDI molecule.[38b]

The temperature dependence of the transfer rates observed in Figure 9b relates to eq 25, where the temperature is a direct parameter but where λ_s is also temperature-dependent in consequence of the temperature dependence of n and ε_r (eq 24). The temperature dependence is mainly determined by T and λ_s(T) in the exponential factor of eq 25. We have used temperature-dependent values for $\varepsilon_r(T)$ as well as $n(T)$ for TOL and CB (see the Supporting Information, Table S4) to obtain $\lambda_s(T)$.[77−79]

The experimental changes in rates and barriers with temperature for the forward electron transfer and back electron transfer processes are qualitatively reflected by the Jortner model (Figure 9b) using a temperature-independent V_{S_1}−CT = 6 meV ($=48$ cm^{-1}) for TOL and CB. Using the temperature-dependent rates from eq 25 and applying Eyring's eq 16, we determined the ΔG of the CT state and its transition state with respect to $E(S_1)$ at different temperatures (Table S5 of the Supporting Information and Figure 10). Figure 10 shows that the 20 meV lower barrier for electron transfer ($\Delta G^{\#}_{ET}$) found for PDI-PMI in TOL as compared to CB is not predicted by the Marcus−Jortner model, which results in a 30 meV higher $\Delta G^{\#}_{ET}$ in TOL than in CB at $T = 300$ K. We consider such small differences within the error of the model and the parameters chosen.

For the charge recombination rate to the singlet ground state (CT→S_0, k_{NR2}), ΔG_0 equals $-E(S_1) - \Delta G_{ET}$ in eq 25 and V_{CT-S_0} denotes the electronic coupling between the CT and the S_0 state. While for both solvents the differences between the predicted and the measured values of $\Delta G^{\#}_{ET}$ and $\Delta G^{\#}_{BET}$ are only minor, a large discrepancy is found between the predicted and the measured values of $\Delta G^{\#}_{CR}$ if only charge recombination to the singlet ground state is accounted for (Figure 10). The discrepancy between the predicted and the measured value of $\Delta G^{\#}_{CR}$ amounts to 0.84 eV in TOL and to 0.13 eV in CB (Figure 10). This is also reflected by the differences between the observed k_{CR} and the predicted rates for k_{NR2}, which are, for example, 20−30× lower in TOL ($6-8\times10^{-3}$ ns^{-1}), at each temperature (Figure 9b), when using a coupling constant ($V_{CT-S_0} = 6$ meV) with a magnitude similar to that between the S_1 and the CT state. These differences between the experimental finding and the theoretical prediction correspond to the experimental results that the CT state is partially depopulated via ISC to the lowest excited triplet state, resulting in a higher k_{CR} than the rate (k_{NR2}) predicted by the model.

Marcus−Jortner Model Including ISC. For charge recombination of the singlet CT state to the charge neutral triplet manifold (k_{T2}, ^{1}CT→T_1), ΔG_0 equals $E(T_1) - E(S_1) - \Delta G_{ET}$. A coupling constant ($V_{CT-T_1} = 6$ meV) with a magnitude similar to V_{S_1}−CT can be used in eq 25 to predict a theoretical rate ($k_{T2}^{TOL} = 145$ and $k_{T2}^{CB} = 500$ ns^{-1}), if it would be an allowed transition. Obviously, these values are orders of magnitude higher than those measured ($k_{T2} = 0.1-0.7$ ns^{-1}), because ^{1}CT→T_1 is indeed spin-forbidden. Two mechanisms have been proposed for ISC via states with CT character (k_{T2}, ^{1}CT→T_1), RP-ISC and SO-ISC. RP-ISC involves ISC from the singlet CT state (or radical pair) to the corresponding triplet CT state (^{1}CT→^{3}CT), followed by charge recombination yielding the locally excited triplet state (^{3}CT→T_1). The second step is a fast process, because it is spin-allowed. It can be described with the rates [k_{T2}(^{3}CT→T_1) on the order of 100 ns^{-1}] mentioned before. Hence, in this mechanism, the first step (^{1}CT→^{3}CT) should be rate-determining and of the order of 0.1 ns^{-1}. Even though at short distances the exchange energy is much larger that the HFI, this mechanism cannot be ruled out.

The SO-ISC mechanism involves a coupled electron transfer and spin inversion, directly converting the ^{1}CT to the T_1 state. SO-ISC can therefore be described by Marcus−Jortner theory if a lower coupling constant is used between the electronic states, ^{1}CT and T_1. Thus, by making use of the measured rates (k_{T2}^{Sol}, Table 4), we obtain $V_{CT-T_1}^{TOL} = 0.13-0.20$ meV and $V_{CT-T_1}^{CB} = 0.09-0.22$ meV, which are ∼40× lower than V_{S_1}−CT^{Sol}. Interestingly, these values are in the same range for the two solvents, which would be expected as the electronic coupling

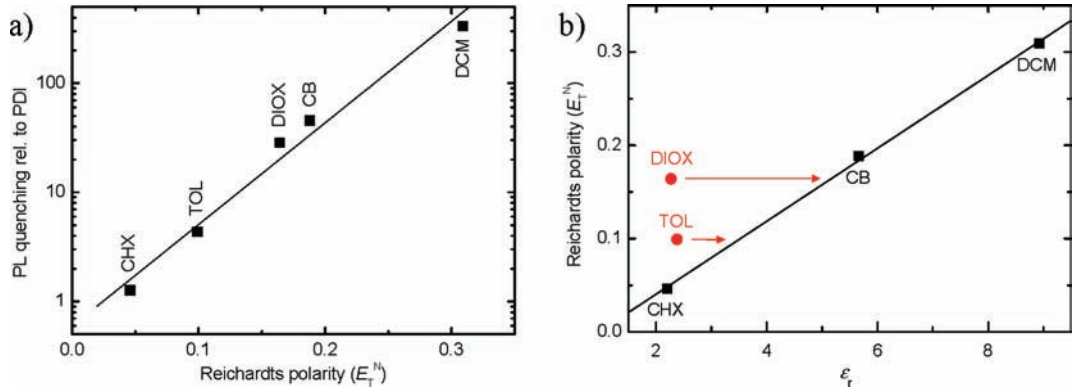

Figure 12. (a) Fluorescence quenching ($I_0/I = \Phi_F^{-1}$) vs Reichardt's polarity (E_T^N). The line is a linear fit to the data. (b) Reichardt's polarity vs relative permittivity (ε_r) of the solvents.

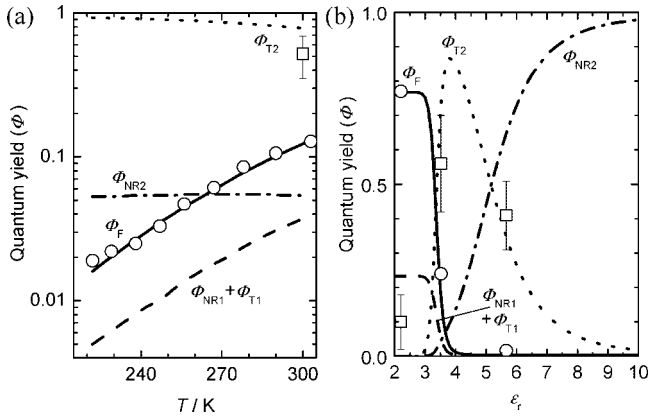

Figure 13. (a) Predicted (lines) temperature dependence of Φ_F, $\Phi_{T1} + \Phi_{NR1}$, Φ_{T2}, and Φ_{NR2} in TOL as compared to those measured for Φ_F (○, from TR-PL, Table S2 of the Supporting Information) and Φ_{T2} (□, Table 4). The values for Φ_{NR2} and $\Phi_{T1} + \Phi_{NR1}$ are within the experimentally obtained ranges: 0−0.34 and 0−0.07, respectively, at $T = 300$ K. (b) Predicted (lines) dependence of Φ_F, $\Phi_{T1} + \Phi_{NR1}$, Φ_{T2}, and Φ_{NR2} on ε_r at $T = 300$ K using $n = 1.500$ and $E(S_1) = 2.25$ eV. Φ_F (○) and Φ_Δ (□, lower limit for $\Phi_{T1} + \Phi_{T2}$) are also plotted for CHX, TOL, and CB (Table 4). For panels a and b, the coupling constants given in the caption of Table 4 were used.

is expected to be roughly solvent-independent. From k_{NR2}, we can only obtain upper limits for V_{CT-S_0} ($V_{CT-S_0}^{TOL} = 0-18$ meV and $V_{CT-S_0}^{CB} = 0-6$ meV); however, because of the electronic similarity between the S_0 and the S_1 state, we can expect that $V_{CT-S_0}^{Sol}$ is of similar magnitude as $V_{S_1-CT}^{Sol}$ (6 meV) rather than the ∼0.17 meV found for $V_{CT-T_1}^{Sol}$.

Previous analyses of SO-ISC ($^1CT \rightarrow T_1$) as a charge recombination with low electronic coupling using the Marcus−Jortner model have revealed electronic coupling constants for other D−A systems. Kobori et al. found $V_{CT-T_1} = 1.6$ cm^{-1} = 0.20 meV for a porphyrin−C_{60} dyad,[80] similar to our results. Gould et al.,[81] however, found a ∼10× lower electronic coupling between ^1CT and T_1 than observed by us ($V_{CT-T_1} = 0.23$ cm^{-1} = 0.028 meV) in a series of CT complexes and 3000× lower than the coupling constant between ^1CT and S_0 ($V_{CT-S_0} = 750$ cm^{-1} = 93 meV). Similar values for V_{CT-T_1} were found by Morais et al. ($V_{CT-S_0} = 1250$ cm^{-1} = 155 meV and $V_{CT-T_1} = 0.18$ cm^{-1} = 0.022 meV) for a small and structurally constrained anthraquinone-based D−A dyad.[30] Thus, for small dyads with strong electronic coupling between ^1CT and S_0 (the CT complexes and the anthraquinone-based dyad), a ca. 10× smaller coupling (V_{CT-T_1}) between the ^1CT and the T_1 is found than for the larger porphyrin−C_{60} dyad and PDI-PMI. These differences could tentatively be explained with the less structurally constrained position of the chromophores in the two larger dyads, thereby also allowing a near perpendicular orientation of D and A to occur, which is beneficial for the SO-ISC rate.

Using $V_{S_1-CT} = V_{CT-S_0} = 6$ meV and $V_{CT-T_1} = 0.17$ meV, we can derive k_{ET}, k_{BET}, k_{T2}, and k_{NR2}, and the quantum yields are in correspondence to those measured (Table 4). The predicted temperature dependence of Φ_F (solid line in Figure 13a) shows good correspondence to that determined by time-resolved fluorescence (○). The increase in Φ_F^{TOL} with temperature is mainly caused by $k_{BET}^{TOL}(T)$, which has a much stronger temperature dependence than either of the other rates. Figure 13b shows the predicted quantum yields as a function of ε_r. The measured data points (Φ_F and Φ_Δ) are indicated in the graph for the three different solvents. Note that Φ_Δ (□) corresponds to a lower limit for $\Phi_{T1} + \Phi_{T2}$. For CHX, the data point is therefore below the curves for $\Phi_{T1} + \Phi_{NR1}$ (dashed). For TOL and CB, the data lie on the predicted line for Φ_{T2} (dotted).

Conclusion and Implications for Solar Cells

We found that in TOL and at $T = 300$ K, the PDI-PMI dyad has a high-energy CT state ($PDI^{-\bullet}$-$PMI^{+\bullet}$) that is nearly isoenergetic ($E_{CT} = 2.19$ eV) to its S_1 state [$E(S_1) = 2.25$ eV]. The small energetic difference combined with a low barrier for electron transfer ($\Delta G_{ET}^{\#} = 130$ meV) allows for a dynamic equilibrium between the S_1 and the CT state that can be described by an electron transfer rate ($S_1 \rightarrow CT$) and a back electron transfer rate ($S_1 \rightarrow CT$) of k_{ET} = ca. 30 ns^{-1} and k_{BET} = 4 ns^{-1}, respectively. In CHX, we find an upward shift of E_{CT} due to the lower polarity of the solvent, and electron transfer ($S_1 \rightarrow CT$) does not occur, while in CB, a more polar solvent, E_{CT} is reduced in energy and k_{BET} is strongly hampered. The barriers for the electron transfer and back transfer processes ($\Delta G_{ET}^{\#}$ and $\Delta G_{BET}^{\#}$) and E_{CT} were determined from (temperature-dependent) TR-PL measurements and compare well with predictions using Marcus−Jortner theory, if for TOL an apparent relative permittivity $\varepsilon_{app} = \varepsilon_r + 1.15$ is used. We find that efficient, near quantitative (∼98%) electron transfer can be obtained when $\Delta G_{ET} = E_{CT} - E(S_1) \approx -120$ meV. This is much less than the minimal value the band edge offset ≈ −0.35 eV that is being considered appropriate for D−A blends.[3]

ns-PIA and singlet oxygen ($^1\Delta_g$) luminescence measurements reveal that decay from the CT state partially occurs via population of the T_1 state, leading to absolute triplet quantum yields of $\Phi_T = 0.42-0.76$ in TOL and $\Phi_T = 0.31-0.98$ in CB. These yields are significantly higher than that determined in CHX ($\Phi_T = 0.02-0.23$). The ISC rates ($S_1 \rightarrow T_1$ in CHX and $CT \rightarrow T_1$ in TOL and CB) were determined and are considerably faster from the CT state ($k_{T2}^{TOL} = 0.075-0\text{-}17$ ns^{-1} and $k_{T2}^{CB} = 0.1-0.7$ ns^{-1}) than from the S_1 state ($k_{T1}^{CHX} = 0.006-0.074$ ns^{-1}) and are actually competing with nonradiative decay to the singlet ground state (S_0). If k_{T2} ($^1CT \rightarrow T_1$) is described by SO-ISC, we find an electronic coupling between the ^1CT and the T_1 state of V_{CT-T_1} = ca. 0.15 meV in TOL and CB, ca. 40 × lower than that between S_1 and ^1CT. In combination with electronic coupling constants for the coupling between the S_1 and the ^1CT state and the ^1CT and the S_0 state ($V_{S_1-CT} = V_{CT-S_0} = 6$ meV), the electronic processes between the four states (S_1, ^1CT, T_1, and S_0) can be described by Marcus−Jortner theory, nearly quantitatively corresponding to the measured values. The recombination to the triplet state is a direct consequence of the high-energy CT state.

The characteristics of PDI-PMI are favorable to serve as a model compound for systems with a low driving force for electron transfer, ΔG_{ET}, creating a high energy CT state in an environment (TOL) with low relative permittivity. Hence, it is interesting to compare the electronic properties of our dyad to those of organic (polymeric) electron donor−acceptor blends used for photovoltaic applications. PDI-PMI approaches such polymer blends in many ways: (i) ε_r of TOL and CB compare well to those of many conjugated polymers ($\varepsilon_r = 2-4$);[1] (ii) the optical gap of 2.2 eV is only ∼0.2−0.3 eV above that of commonly used polymers such as MDMO-PPV {poly[2-methoxy-5-(3′,7′-dimethyloctyloxy)-1,4-phenylene vinylene]} and P3HT [poly(3-hexylthiophene)];[1] (iii) the low ΔG_{ET} compares to a situation that is aimed for in such blends, because it makes E_{CT} as high as possible for a given optical gap and for photovoltaic devices the open-circuit voltage (V_{OC}) is linearly dependent on E_{CT};[12,13c,82] (iv) photovoltaic devices typically operate near $T = 300$ K; and (v) the fluorescent lifetime of the separate chromophores compares to that of the individual materials in such blends. Of course, a molecular dyad in solution is a simple model for a blend film. The largest differences

between our model compound and a polymer blend are (i) the relatively low electronic overlap between the wave functions of the dyad as compared to the close-packed chromophores in a film, (ii) the low viscosity of the medium (liquid), allowing for molecular reorganizations that occur less in polymeric blends, and (iii) the impossibility for the photogenerated charges to dissociate over longer distances than the size of the molecule (~2 nm). We will compare two aspects of the properties of our PDI-PMI dyad to that of electron donor−acceptor blends. First, the limit for ΔG_{ET} will be considered, and then, the triplet formation in PDI-PMI will be compared to that in polymer blends.

Photoexcitation of PDI-PMI in TOL ($\Delta G_{ET} = -50$ meV) and CB ($\Delta G_{ET} = -150$ meV) is followed by a fast forward electron transfer ($S_1 \rightarrow CT$), depopulating the singlet excited state faster than fluorescent decay (k_{ET} = ca. 100 × k_F for both solvents), despite the low ΔG_{ET}. This is enabled by the low barriers for electron transfer ($\Delta G_{ET}^{\#}$ = ca. 150 meV). However, back electron transfer from the CT to the S_1 state (k_{BET}, $S_1 \rightarrow CT$) can also be fast at such low driving forces and actually acts as a depopulation route for the CT state of PDI-PMI in TOL, which can easily be visualized by the relatively high PL yield (Φ_F from S_1) of ca. 20%. In CB ($\Phi_F < 0.02$) the back electron transfer rate (k_{BET}) is negligible, which is supported by TR-PL and ps-PIA measurements.

Back electron transfer from CT to S_1 has been reported for electron donor−acceptor blends of conjugated polymers with a small driving force for electron transfer, that is, with small HOMO or LUMO offsets. Morteani et al. used the term "efficient electron−hole capture" for the repopulation of the S_1 state of the polymer with the lowest optical band gap from injected holes and electrons from the HOMO of the electron donor and LUMO of the electron acceptor, respectively, and used this process to prepare efficient LEDs.[10c,83]

For PDI-PMI, however, the results clearly show that a high E_{CT} allows decay from the CT state to the lower energy triplet state ($CT \rightarrow T_1$). Notably, if the CT state of PDI-PMI is populated (in TOL and CB), much higher triplet quantum yields (Φ_T = 0.3−1) are found than for the reference compounds PDI and PMI and than for PDI-PMI in CHX (Φ_T = 0.02−0.23) in which the CT state is not populated. Not only the triplet quantum yields are much higher in TOL and CB, also the ISC rates (0.1−0.7 ns^{-1}) are an order of magnitude faster than in CHX (0.01−0.07 ns^{-1}) and are strongly competing with nonradiative decay to the ground state (k_{NR2} = 0−0.5 ns^{-1}).

Also, in polymer:polymer[13] and polymer:PCBM[12,14] blends for organic photovoltaics, enhanced triplet formation via the CT state is observed in some cases, generally for blends with low HOMO and LUMO offset, thus a small driving force for electron transfer, and consequentially a high E_{CT} (and high V_{OC} for the photovoltaic devices). Thus, although the high V_{OC} is beneficial for device performance, the high E_{CT} makes recombination to lower lying triplet states of either of the two materials more favorable, thereby shortening the decay time of the CT state. The results of the PDI-PMI dyad show that in such a situation recombination to the triplet manifold can be a major decay pathway. It would therefore be desirable to design materials with a small energy difference between the lowest singlet exciton state [$E(S_1)$] and the lowest triplet excited state [$E(T_1)$]. Such materials with a low singlet−triplet splitting [$E_{ST} = E(S_1) - E(T_1)$] would be ideal candidates to achieve high-energy CT states at an energy just below $E(S_1)$, thereby allowing for a high V_{OC}, without compromising on the decay time, because charge recombination to a low lying triplet state is prevented if $E_{CT} < E(T_1)$.

Acknowledgment. We thank Professor K. Müllen (Mainz) for a generous gift of compound **1**. This work was supported by the EU Integrated Project NAIMO (No. NMP4-CT-2004-500355).

Supporting Information Available: Further details on oxygen phosphorescence, temperature-dependent rate constants and energy barriers, and an analysis of the solvatochromism of PMI, PDI, and PDI-PMI. This material is available free of charge via the Internet at http://pubs.acs.org.

References and Notes

(1) (a) Coakley, K. M.; McGehee, M. D. *Chem. Mater.* **2004**, *16*, 4533–4542. (b) Günes, S.; Neugebauer, H.; Sariciftci, N. S. *Chem. Rev.* **2007**, *107*, 1324–1338.

(2) Brédas, J. L.; Beljonne, D.; Coropceanu, V.; Cornil, J. *Chem. Rev* **2004**, *104*, 4971–5003.

(3) (a) Halls, J. J. M.; Cornil, J.; dos Santos, D. A.; Silbey, R.; Hwang, D.-H.; Holmes, A. B.; Brédas, J. L.; Friend, R. H. *Phys. Rev. B* **1999**, *60*, 5721. (b) Veldman, D.; Bastiaansen, J. J. A. M.; Langeveld-Voss, B. M. W.; Sweelssen, J.; Koetse, M. M.; Meskers, S. C. J.; Janssen, R. A. J. *Thin Solid Films* **2006**, *511−512*, 581–586. (c) Liu, Y.; Scully, S. R.; McGehee, M. D.; Liu, J.; Luscombe, C. K.; Fréchet, J. M. J.; Shaheen, S. E.; Ginley, D. S. *J. Phys. Chem. B* **2006**, *110*, 3257–3261.

(4) (a) Beens, H.; Knibbe, H.; Weller, A. *J. Chem. Phys.* **1967**, *47*, 1183–1184. (b) Weller, A. *Z. Phys. Chem.* **1982**, *133*, 93–98.

(5) (a) Montanari, I.; Nogueira, A. F.; Nelson, J.; Durrant, J. R.; Winder, C.; Loi, M. A.; Sariciftci, N. S.; Brabec, C. *Appl. Phys. Lett.* **2002**, *81*, 3001–3003. (b) Nogueira, A. F.; Montanari, I.; Nelson, J.; Durrant, J. R.; Winder, C.; Sariciftci, N. S. *J. Phys. Chem. B* **2003**, *107*, 1567–1573. (c) Offermans, T.; Meskers, S. C. J.; Janssen, R. A. J. *J. Chem. Phys.* **2003**, *119*, 10924–10929. (d) Kim, Y.; Cook, S.; Choulis, S. A.; Nelson, J.; Durrant, J. R.; Bradley, D. D. C. *Chem. Mater.* **2004**, *16*, 4812–4818. (e) Offermans, T.; Meskers, S. C. J.; Janssen, R. A. J. *Chem. Phys.* **2005**, *308*, 125–133.

(6) De, S.; Pascher, T.; Maiti, M.; Jespersen, K. G.; Kesti, T.; Zhang, F.; Inganäs, O.; Yartsev, A.; Sundström, V. *J. Am. Chem. Soc.* **2007**, *129*, 8466–8472.

(7) (a) Hasharoni, K.; Keshavarz-K., M.; Sastre, A.; Gonzalez, R.; Bellavia-Lund, C.; Greenwald, Y. J. *Chem. Phys.* **1997**, *107*, 2308–2312. (b) Kim, H.; Kim, J. Y.; Park, S. H.; Lee, K.; Jin, Y.; Kim, J.; Suh, H. *Appl. Phys. Lett.* **2005**, *86*, 183502.

(8) Benson-Smith, J. J.; Goris, L.; Vandewal, K.; Haenen, K.; Manca, J. V.; Vanderzande, D.; Bradley, D. D. C.; Nelson, J. *Adv. Funct. Mater.* **2007**, *17*, 451–457.

(9) Loi, M. A.; Toffanin, S.; Muccini, M.; Forster, M.; Scherf, U.; Scharber, M. *Adv. Funct. Mater.* **2007**, *17*, 2111–2116.

(10) (a) Alam, M. M.; Jenekhe, S. A. *J. Phys. Chem. B* **2001**, *105*, 2479–2482. (b) Zhang, X. J.; Kale, D. M.; Jenekhe, S. A. *Macromolecules* **2002**, *35*, 382–393. (c) Morteani, A. C.; Dhoot, A. S.; Kim, J.-S.; Silva, C.; Greenham, N. C.; Murphy, C.; Moons, E.; Ciná, S.; Burroughes, J. H.; Friend, R. H. *Adv. Mater.* **2003**, *15*, 1708–1712. (d) Morteani, A. C.; Sreearunothai, P.; Herz, L. M.; Friend, R. H.; Silva, C. *Phys. Rev. Lett.* **2004**, *92*, 247402. (e) Kietzke, T.; Neher, D.; Hörhold, H.-H. *Chem. Mater.* **2005**, *17*, 6532–6537. (f) Chasteen, S. V.; Haerter, J. O.; Rumbles, G.; Scott, J. C.; Nakazawa, Y.; Jones, M.; Hörhold, H.-H.; Tillmann, H.; Carter, S. A. *J. Appl. Phys.* **2006**, *99*, 033709. (g) Yin, C.; Kietzke, T.; Neher, D.; Hörhold, H.-H. *Appl. Phys. Lett.* **2007**, *90*, 092117.

(11) Offermans, T.; van Hal, P. A.; Meskers, S. C. J.; Koetse, M. M.; Janssen, R. A. J. *Phys. Rev. B* **2005**, *72*, 045213.

(12) Veldman, D.; Ipek, Ö.; Meskers, S. C. J.; Sweelssen, J.; Koetse, M. M.; Veenstra, S. C.; Kroon, J. M.; van Bavel, S. S.; Loos, J.; Janssen, R. A. J. *J. Am. Chem. Soc.* **2008**, *130*, 7721–7735.

(13) (a) Ford, T. A.; Avilov, I.; Beljonne, D.; Greenham, N. C. *Phys. Rev. B* **2005**, *71*, 125212. (b) Offermans, T.; van Hal, P. A.; Meskers, S. C. J.; Koetse, M. M.; Janssen, R. A. J. *Phys. Rev. B* **2005**, *72*, 045213. (c) Veldman, D.; Offermans, T.; Sweelssen, J.; Koetse, M. M.; Meskers, S. C. J.; Janssen, R. A. J. *Thin Solid Films* **2006**, *511−512*, 333–337.

(14) (a) Ohkita, H.; Cook, S.; Astuti, Y.; Duffy, W.; Heeney, M.; Tierney, S.; McCulloch, I.; Bradley, D. D. C.; Durrant, J. R. *Chem. Commun.* **2006**, *3939*, 3941. (b) Ohkita, H.; Cook, S.; Astuti, Y.; Duffy, W.; Tierney, S.; Zhang, W.; Heeney, M.; McCulloch, I.; Nelson, J.; Bradley, D. D. C.; Durrant, J. R. *J. Am. Chem. Soc.* **2008**, *130*, 3030–3042.

(15) (a) Fron, E.; Schweitzer, G.; Jacob, J.; van Vooren, A.; Beljonne, D.; Müllen, K.; Hofkens, J.; van der Auweraer, M.; de Schryver, F. C. *ChemPhysChem* **2007**, *8*, 1386–1393. (b) Fron, E.; Bell, T. D. M.; van

Vooren, A.; Schweitzer, G.; Cornil, J.; Beljonne, D.; Toele, P.; Jacob, J.; Müllen, K.; Hofkens, J.; van der Auweraer, M.; de Schryver, F. C. *J. Am. Chem. Soc.* **2007**, *129*, 610–619.

(16) Kawatsu, T.; Coropceanu, V.; Ye, A.; Brédas, J.-L. *J. Phys. Chem. C* **2008**, *112*, 3429–3433.

(17) Verhoeven, J. W. *J. Photochem. Photobiol. C: Photochem. Rev.* **2006**, *7*, 40–60.

(18) Dance, Z. E. X.; Mi, Q.; McCamant, D. W.; Ahrens, M. J.; Ratner, M. A.; Wasielewski, M. R. *J. Phys. Chem. B* **2006**, *110*, 25163–25173.

(19) Wasielewski, M. R.; Johnson, D. G.; Svec, W. A.; Kersey, K. M.; Minsek, D. W. *J. Am. Chem. Soc.* **1988**, *110*, 7219–7221.

(20) Wiederrecht, G. P.; Svec, W. A.; Wasielewski, M. R.; Galili, T.; Levanon, H. *J. Am. Chem. Soc.* **2000**, *122*, 9715–9722.

(21) (a) Dutton, P. L.; Leigh, J. S.; Seibert, M. *Biochem. Biophys. Res. Commun.* **1972**, *46*, 406–413. (b) Thurnauer, M. C.; Katz, J. J.; Norris, J. R. *Proc. Natl. Acad. Sci. U.S.A.* **1975**, *72*, 3270–3274. (c) Levanon, H.; Norris, J. R. *Chem. Rev.* **1978**, *78*, 185–198.

(22) (a) Hasharoni, K.; Levanon, H.; Greenfield, S. R.; Gosztola, D. J.; Svec, W. A.; Wasielewski, M. R. J. *J. Am. Chem. Soc.* **1995**, *117*, 8055–8056. (b) Carbonera, D.; DiValentin, N.; Corvaja, C.; Agostini, G.; Giacometti, G.; Liddell, P. A.; Kuciauskas, D.; Moore, A. L.; Moore, T. A.; Gust, D. *J. Am. Chem. Soc.* **1998**, *120*, 4398–4405.

(23) Okada, T.; Karaki, I.; Matsuzawa, E.; Mataga, N.; Sakata, Y.; Misumi, S. *J. Phys. Chem.* **1981**, *85*, 3957–3960.

(24) van Willigen, H.; Jones, G.; Farahat, M. S. *J. Phys. Chem.* **1996**, *100*, 3312–3316.

(25) (a) Benniston, A. C.; Harriman, A.; Li, P.; Rostron, J. P.; Verhoeven, J. W. *Chem. Commun.* **2005**, *2701*, 2703. (b) Benniston, A. C.; Harriman, A.; Li, P.; Rostron, J. P.; van Ramesdonk, H. J.; Groeneveld, M. M.; Zhang, H.; Verhoeven, J. W. *J. Am. Chem. Soc.* **2005**, *127*, 16054–16064.

(26) Harriman, A.; Mallon, L. J.; Ulrich, G.; Ziessel, R. *ChemPhysChem* **2007**, *8*, 1207–1214.

(27) Lor, M.; Thielemans, J.; Viaene, L.; Cotlet, M.; Hofkens, J.; Weil, T.; Hampel, C.; Müllen, K.; Verhoeven, J. W.; van der Auweraer, M.; de Schryver, F. C. *J. Am. Chem. Soc.* **2002**, *124*, 9918–9925.

(28) Cotlet, M.; Masuo, S.; Lor, M.; Fron, E.; van der Auweraer, M.; Müllen, K.; Hofkens, J.; de Schryver, F. C. *Angew. Chem., Int. Ed.* **2004**, *43*, 6116–6120.

(29) Luo, C.; Guldi, D. M.; Imahori, H.; Tamaki, K.; Sakata, Y. *J. Am. Chem. Soc.* **2000**, *122*, 6535–6551.

(30) Morais, J.; Hung, R. R.; Grabowski, J. J.; Zimmt, M. B. *J. Phys. Chem.* **1993**, *97*, 13138–13144.

(31) Khudyakov, I. V.; Serebrennikov, Y. A.; Turro, N. J. *Chem. Rev.* **1993**, *93*, 537–570.

(32) Vosch, T.; Hofkens, J.; Cotlet, M.; Köhn, F.; Fujiwara, H.; Gronheid, R.; van der Biest, K.; Weil, T.; Herrmann, A.; Müllen, K.; Mukamel, S.; van der Auweraer, M.; de Schryver, F. C. *Angew. Chem., Int. Ed.* **2001**, *40*, 4643–4648.

(33) Tinnefeld, P.; Hofkens, J.; Herten, D. P.; Masuo, S.; Vosch, T.; Cotlet, M.; Habuchi, S.; Müllen, K.; de Schryver, F. C.; Sauer, M. *ChemPhysChem* **2004**, *5*, 1786–1790.

(34) Holman, M. W.; Yan, P.; Ching, K.-C.; Liu, R.; Ishak, F. I.; Adams, D. M. *Chem. Phys. Lett.* **2005**, *413*, 501–503.

(35) Cioslowski, J.; Piskorz, P.; Liu, G.; Moncrieff, D. *J. Phys. Chem.* **1996**, *100*, 19333–19335.

(36) Langhals, H. *Helv. Chim. Acta* **2005**, *88*, 1309–1343.

(37) Langhals, H.; Jona, W. *Angew. Chem., Int. Ed.* **1998**, *37*, 952–955.

(38) (a) Liu, R.; Holman, M. W.; Zang, L.; Adams, D. M. *J. Phys. Chem. A* **2003**, *107*, 6522–6526. (b) Holman, M. W.; Liu, R.; Zang, L.; Yan, P.; DiBenedetto, S. A.; Bowers, R. D.; Adams, D. M. *J. Am. Chem. Soc.* **2004**, *126*, 16126–16133. (c) Holman, M. W.; Yan, P.; Adams, D. M.; Westenhoff, S.; Silva, C. *J. Phys. Chem. A* **2005**, *109*, 8548–8552.

(39) Lukas, A. S.; Zhao, Y.; Miller, S. E.; Wasielewski, M. R. *J. Phys. Chem. B* **2002**, *106*, 1299–1306.

(40) Neuteboom, E. E.; Meskers, S. C. J.; Beckers, E. H. A.; Chopin, S.; Janssen, R. A. J. *J. Phys. Chem. A* **2006**, *110*, 12363–12371.

(41) Fuller, M. J.; Gusev, A. V.; Wasielewski, M. R. *Isr. J. Chem.* **2004**, *44*, 101–108.

(42) Leroy-Lhez, S.; Perrin, L.; Baffreau, J.; Hudhomme, P. C. R. *Chimie* **2006**, *9*, 240–246.

(43) Cotlet, M.; Masuo, S.; Luo, G.; Hofkens, J.; van der Auweraer, M.; Verhoeven, J. W.; Müllen, K.; Xie, S. X.; de Schryver, F. C. *Proc. Natl. Acad. Sci.* **2004**, *101*, 14343–14348.

(44) Ford, W. E.; Kamat, P. V. *J. Phys. Chem.* **1987**, *91*, 6373–6380.

(45) Kircher, T.; Löhmannsröben, H.-G. *Phys. Chem. Chem. Phys.* **1999**, *1*, 3987–3992.

(46) Langhals, H.; Jona, W. *Chem. Eur. J.* **1998**, *4*, 2110–2116.

(47) Quante, H.; Müllen, K. *Angew. Chem., Int. Ed.* **1995**, *34*, 1323–1325.

(48) Kaiser, H.; Lindner, J.; Langhals, H. *Chem. Ber* **1991**, *124*, 529–535.

(49) The low PL quantum yield causes a low contribution (A_1) of τ_1, by itself causing a higher inaccuracy. Furthermore, a low amount (e.g., <0.05% of residual PDI) of fluorescent impurity may at these low PL quantum yields have a substantial effect of A_1/A_2 and thus on k_{BET}. Also, it may affect τ_1 and thus k_{CR}.

(50) Schmidt, R.; Afshari, E. *J. Phys. Chem.* **1990**, *94*, 4377–4378.

(51) Scurlock, R. D.; Nonell, S.; Braslavsky, S. E.; Ogilby, P. R. *J. Phys. Chem.* **1995**, *99*, 3521–3526.

(52) Arbogast, J. W.; Darmanyan, A. P.; Foote, C. S.; Rubin, Y.; Diederich, F. N.; Alvarez, M. M.; Anz, S. J.; Whetten, R. L. *J. Phys. Chem.* **1991**, *95*, 11–12.

(53) Terazima, M.; Hirota, N.; Shinohara, H.; Saito, Y. *J. Phys. Chem.* **1991**, *95*, 9080–9085.

(54) Schmidt, R.; Tanielian, C. *J. Phys. Chem. A* **2000**, *104*, 3177–3180.

(55) According to Schmidt et al. (ref 54), special care must be taken for TPP in benzene, as the oxygen ($1\Delta_g$) luminescence may deviate early from linearity.

(56) As explained by Beeby et al. (ref 57), this may cause such signals that even extend to a few microseconds. For TPP, similar signals were reported by Schmidt et al. (ref 54).

(57) Beeby, A.; Parker, A. W.; Stanley, C. F. *J. Photochem. Photobiol., B* **1997**, *37*, 267–271.

(58) Miyaura, N.; Suzuki, A. *Chem. Rev.* **1995**, *95*, 2457–2483.

(59) Maus, M.; Mitra, S.; Lor, M.; Hofkens, J.; Weil, T.; Herrmann, A.; Müllen, K.; de Schryver, F. C. *J. Phys. Chem. A* **2001**, *105*, 3961–3966.

(60) (a) Kasha, M.; Rawls, H. R.; El-Bayoumi, M. A. *Pure Appl. Chem.* **1965**, *11*, 371–392. (b) Fulton, R. L.; Gouterman, M. *J. Chem. Phys.* **1964**, *41*, 2280–2286. (c) Oddos-Marcel, L.; Madeore, F.; Bock, A.; Neher, D.; Ferencz, A.; Rengel, H.; Wegner, G.; Kryschi, C.; Trommsdorff, H. P. *J. Phys. Chem.* **1996**, *100*, 11850–11856.

(61) Langhals, H.; Karolin, J.; Johansson, L. B.-Å. *J. Chem. Soc. Faraday Trans.* **1998**, *94*, 2919–2922.

(62) Ware, W. R.; Watt, D.; Holmes, J. D. *J. Am. Chem. Soc.* **1974**, *96*, 7853–7860.

(63) (a) Ford, W. E.; Hiratsuka, H.; Kamat, P. V. *J. Phys. Chem.* **1989**, *93*, 6692–6696. (b) Salbeck, J. *J. Electroanal. Chem.* **1992**, *340*, 169–195.

(64) Schweitzer, C.; Schmidt, R. *Chem. Rev.* **2003**, *103*, 1685–1757.

(65) Reynolds, L.; Gardecki, J. A.; Frankland, S. J. V.; Horng, M. L.; Maroncelli, M. *J. Phys. Chem.* **1996**, *100*, 10337–10354.

(66) Reichardt, C. *Chem. Rev.* **1994**, *94*, 2319–2358.

(67) Jeon, J.; Kim, H. J. *J. Solution Chem.* **2001**, *30*, 849–860.

(68) Matyushov, D. V.; Voth, G. A. *J. Chem. Phys.* **1999**, *111*, 3630–3638.

(69) Geerlings, J. D.; Varma, C. A. G. O.; Hemert, M. C. van. *J. Phys. Chem. B* **2000**, *104*, 56–64.

(70) Dorairaj, S.; Kim, H. J. *J. Phys. Chem. A* **2002**, *106*, 2322–2327.

(71) Khajehpour, M.; Kaufmann, J. F. *J. Phys. Chem. A* **2001**, *105*, 10316–10321.

(72) ϵ_{app} is strongly dependent on the size (radius) of the solute, because quadrupolar interactions are short-range (refs 67 and 68). For larger solutes, a lower effect of the quadrupole moment and a smaller ϵ_{app} are anticipated.

(73) Marcus, R. A. *J. Chem. Phys.* **1965**, *43*, 679–701.

(74) (a) Kestner, N. R.; Logan, J.; Jortner, J. *J. Phys. Chem.* **1974**, *78*, 2148–2166. (b) Ulstrup, J.; Jortner, J. *J. Chem. Phys.* **1975**, *63*, 4358–4368. (c) Jortner, J., Bixon, M., Eds. *Electron Transfer: From Isolated Molecules to Biomolecules*; Adv. Chem. Phys. Series; Wiley: New York, 1999; Vols. *106*−*107*.

(75) (a) Oevering, H.; Paddon-Row, M. N.; Heppener, M.; Oliver, A. M.; Cotsaris, E.; Verhoeven, J. W.; Hush, N. S. *J. Am. Chem. Soc.* **1987**, *109*, 3258–3269. (b) Kroon, J.; Verhoeven, J. W.; Paddon-Row, M. N.; Oliver, A. M. *Angew. Chem., Int. Ed.* **1991**, *30*, 1358–1361.

(76) Kroon, J.; Oevering, H.; Verhoeven, J. W.; Warman, J. M.; Oliver, A. M.; Paddon-Row, M. N. *J. Phys. Chem.* **1993**, *97*, 5065–5069.

(77) Lide, D. R., Ed. *CRC Handbook of Chemistry and Physics*, 88th ed. (Internet Version 2008); CRC Press/Taylor and Francis: Boca Raton, FL, 2008.

(78) El-Kashef, H. *Physica B* **2002**, *311*, 376–379.

(79) Rubio, J. E. F.; Arsuaga, J. M.; Taravillo, M.; Baonza, V. G.; Cáceres, M. *Exp. Therm. Fluid Sci.* **2004**, *28*, 887–891.

(80) Kobori, Y.; Yamauchi, S.; Akiyama, K.; Tero-Kubota, S.; Imahori, H.; Fukuzumi, S.; Norris, J. R., Jr. *Proc. Natl. Acad. Sci. U.S.A.* **2005**, *102*, 10017–10022.

(81) Gould, I. R.; Boiani, J. A.; Gaillard, E. B.; Goodman, J. L.; Farid, S. *J. Phys. Chem. A* **2003**, *107*, 3515–3524.

(82) (a) Brabec, C. J.; Cravino, A.; Meissner, D.; Sariciftci, N. S.; Fromherz, T.; Rispens, M. T.; Sanchez, L.; Hummelen, J. C. *Adv. Funct. Mater.* **2001**, *11*, 374–379. (b) Gadisa, A.; Svensson, M.; Andersson, M. R.; Inganäs, O. *Appl. Phys. Lett.* **2004**, *84*, 1609–1611. (c) Cremer, J.; Bäuerle, P.; Wienk, M. M.; Janssen, R. A. J. *Chem. Mater.* **2006**, *18*, 5832–5834. (d) Roquet, S.; Cravino, A.; Leriche, P.; Alévéque, O.; Frère, P.; Roncali, J. *J. Am. Chem. Soc.* **2006**, *128*, 3459–3466. (e) Mutolo, K. L.; Mayo, E. I.;

Rand, B. P.; Forrest, S. R.; Thompson, M. E. *J. Am. Chem. Soc.* **2006**, *128*, 8108–8109. (f) Scharber, M. C.; Mühlbacher, D.; Koppe, M.; Denk, P.; Waldauf, C.; Heeger, A. J.; Brabec, C. J. *Adv. Mater.* **2006**, *18*, 789–794. (g) Kooistra, F. B.; Knol, J.; Kastenberg, F.; Popescu, L. M.; Verhees, W. J. H.; Kroon, J. M.; Hummelen, J. C. *Org. Lett.* **2007**, *9*, 551–554. (h) Rand, B. P.; Burk, D. P.; Forrest, S. R. *Phys. Rev. B* **2007**, 115327. (i) Cravino, A. *Appl. Phys. Lett.* **2007**, *91*, 243502. (j) Ishwara, T.; Bradley, D. D. C.; Nelson, J.; Ravirajan, P.; Vanseveren, I.; Cleij, T.; Vanderzande, D.; Lutsen, L.; Tierney, S.; Heeney, M.; McCulloch, I. *Appl. Phys. Lett.* **2008**, *92*, 053308.

(83) Morteani, A. C.; Friend, R. H.; Silva, C. *J. Chem. Phys.* **2005**, *122*, 244906.

JP805949R